

The role of self-supervised pretraining in differentially private medical image analysis

Soroosh Tayebi Arasteh (1,2,3,4), Mina Farajiamiri (1,5), Mahshad Lotfinia (1), Behrus Hinrichs-Puladi (6,7), Jonas Bienzeisler (7), Mohamed Alhaskir (7), Mirabela Rusu (3,4), Christiane Kuhl (2), Sven Nebelung (1,2), Daniel Truhn (1,2)

- (1) Lab for AI in Medicine, RWTH Aachen University, Aachen, Germany.
- (2) Department of Diagnostic and Interventional Radiology, University Hospital RWTH Aachen, Aachen, Germany.
- (3) Department of Urology, Stanford University, Stanford, CA, USA.
- (4) Department of Radiology, Stanford University, Stanford, CA, USA.
- (5) School of Business and Economics, RWTH Aachen University, Aachen, Germany.
- (6) Department of Oral and Maxillofacial Surgery, University Hospital RWTH Aachen, Aachen, Germany.
- (7) Institute of Medical Informatics, University Hospital RWTH Aachen, Aachen, Germany.

Abstract

Differential privacy (DP) provides formal protection for sensitive data but typically incurs substantial losses in diagnostic performance. Model initialization has emerged as a critical factor in mitigating this degradation, yet the role of modern self-supervised learning under full-model DP remains poorly understood. Here, we present a large-scale evaluation of initialization strategies for differentially private medical image analysis, using chest radiograph classification as a representative benchmark with more than 800,000 images. Using state-of-the-art ConvNeXt models trained with DP-SGD across realistic privacy regimes, we compare non-domain-specific supervised ImageNet initialization, non-domain-specific self-supervised DINOv3 initialization, and domain-specific supervised pretraining on MIMIC-CXR, the largest publicly available chest radiograph dataset. Evaluations are conducted across five external datasets spanning diverse institutions and acquisition settings. We show that DINOv3 initialization consistently improves diagnostic utility relative to ImageNet initialization under DP, but remains inferior to domain-specific supervised pretraining, which achieves performance closest to non-private baselines. We further demonstrate that initialization choice strongly influences demographic fairness, cross-dataset generalization, and robustness to data scale and model capacity under privacy constraints. The results establish initialization strategy as a central determinant of utility, fairness, and generalization in differentially private medical imaging.

Correspondence

Soroosh Tayebi Arasteh, Dr.-Ing., Dr. rer. medic. (soroosh.arasteh@rwth-aachen.de)

Lab for AI in Medicine, Department of Diagnostic and Interventional Radiology, University Hospital RWTH Aachen
Pauwelsstr. 30, 52074 Aachen, Germany

This is a pre-print version, submitted to arxiv.org.

January 27, 2026

1. Introduction

The increasing deployment of deep learning models in medical image analysis has intensified concerns about patient privacy, particularly as models are trained on centralized collections of sensitive clinical data. Models trained on medical images are vulnerable to information leakage through attacks such as membership inference and data reconstruction, especially when model weights are shared, deployed across institutions, or reused beyond their original training context^{1–4}. These risks pose significant ethical, legal, and regulatory challenges for the adoption of medical deep learning. Differential privacy (DP)⁵ provides a principled framework to address these concerns by offering formal guarantees that bound the influence of any individual training sample on the learned model. By injecting calibrated noise during training, DP enables the release and deployment of models with quantifiable privacy protection. Despite its strong theoretical foundations, the practical adoption of DP in medical imaging remains limited, largely due to consistent degradation in diagnostic performance^{6,7} and fairness^{1,2,4}, and a lack of clear guidance on how training choices shape achievable utility under privacy constraints^{1,2,4,8–11}.

A central but underexplored factor governing performance under DP is model initialization^{1,4,8,9}. Under differentially private stochastic gradient descent (DP-SGD)¹⁰, optimization dynamics are fundamentally altered by gradient clipping and noise injection, often preventing models from converging to high-performing solutions when trained from scratch. Prior work has shown that strong initialization is frequently essential for achieving usable performance under DP, particularly for convolutional neural networks trained end to end^{1,4,8,9}. In medical imaging, supervised pretraining on large, domain-specific datasets has emerged as one of the most effective strategies for mitigating privacy-induced utility loss. However, this approach depends on access to extensive labeled clinical data, which is often restricted, institution-specific, or costly to curate, limiting its applicability in many realistic settings.

Self-supervised learning (SSL) offers an alternative by enabling representation learning from large-scale unlabeled data^{12,13}. Modern SSL methods have demonstrated strong transfer performance across a wide range of medical imaging tasks^{14–17}, often surpassing ImageNet^{18,19} initialization in non-private training regimes. Whether these advantages extend to fully differentially private training, however, remains unclear. SSL representations are learned without accounting for the constraints imposed by DP, and most prior evaluations have focused on frozen representations or fine-tuning without privacy guarantees. Moreover, many widely adopted SSL models have primarily been released for transformer-based^{20,21} architectures, which remain challenging to train under full-model DP due to optimization instability and memory constraints¹⁷. The recent release of DINOv3 substantially changes this landscape by providing high-quality self-supervised pretrained weights for modern convolutional architectures, including ConvNeXt²². This development enables, for the first time, a systematic investigation of self-supervised initialization for fully differentially private convolutional networks. Importantly, this setting differs fundamentally from prior SSL studies, as pretrained representations must be adapted throughout training under clipped and noisy gradients rather than serving as fixed or lightly fine-tuned features. Whether self-supervised representations learned from natural images can meaningfully support

optimization under DP, and how they compare with both ImageNet and domain-specific supervised initialization, remains an open question.

In this study, as shown in **Figure 1**, we conduct a large-scale, systematic evaluation of initialization strategies for differentially private medical image analysis, using chest radiograph classification as a representative and clinically relevant benchmark^{19,23–25}. We train ConvNeXt-Small models under full-model DP across realistic privacy regimes and compare three initialization strategies: supervised ImageNet pretraining, self-supervised DINOv3²⁶ pretraining, and domain-specific supervised pretraining on the MIMIC-CXR²⁴ dataset, the largest publicly available chest radiograph cohort to date. Models are evaluated on five external chest radiograph datasets spanning 7 institutions, 4 countries across 3 continents, and different acquisition protocols. Beyond diagnostic utility, we analyze demographic fairness across sex and age groups, assess cross-dataset generalization under privacy constraints, and examine how model capacity and training set size interact with privacy to shape achievable performance. Our results demonstrate that initialization is a dominant determinant of utility, fairness, and generalization under DP. Self-supervised DINOv3 initialization consistently improves robustness and performance relative to ImageNet initialization, substantially narrowing the performance gap induced by privacy constraints. However, self-supervised initialization does not fully substitute for domain-specific supervised pretraining, which remains the most effective strategy for preserving utility and stabilizing fairness under DP. Our results clarify the practical strengths and limitations of SSL in privacy-preserving medical imaging and provide actionable guidance for selecting initialization strategies when deploying differentially private models at scale.

2. Results

2.1. Initialization governs diagnostic utility under differential privacy

We first assessed diagnostic performance of ConvNeXt-Small models²² trained with and without DP across five large adult chest radiograph datasets: VinDr-CXR²⁷, ChestX-ray14²⁸, PadChest²⁹, CheXpert²⁵, and UKA-CXR^{1,4,16,17,30–32}. Models were trained to jointly predict five thoracic findings including atelectasis, cardiomegaly, pleural effusion, pneumonia, and no finding. Performance was evaluated using label-averaged area under the receiver operating characteristic curve (AUROC) as the primary metric, with accuracy, sensitivity, and specificity reported as secondary metrics (**Table 1**). Because disease prevalence varies substantially across datasets, we emphasize AUROC, sensitivity, and specificity as prevalence-independent measures, while accuracy is reported for completeness and interpreted in the context of dataset-specific label distributions. Results were compared across three DP ranges and against a non-private baseline (**Figure 2**). Across all datasets, enforcing DP resulted in statistically significant reductions in AUROC relative to non-private training, with all comparisons reaching statistical significance at $P < 0.001$ unless otherwise stated. Importantly, the magnitude of this degradation varied substantially across initialization strategies. Models initialized without task-aligned or domain-relevant pretraining exhibited pronounced performance loss under DP, consistent with the

sensitivity of deep networks to gradient clipping and noise injection. This pattern was consistent across datasets spanning different sizes, label prevalences, and clinical settings (see **Table 1**).

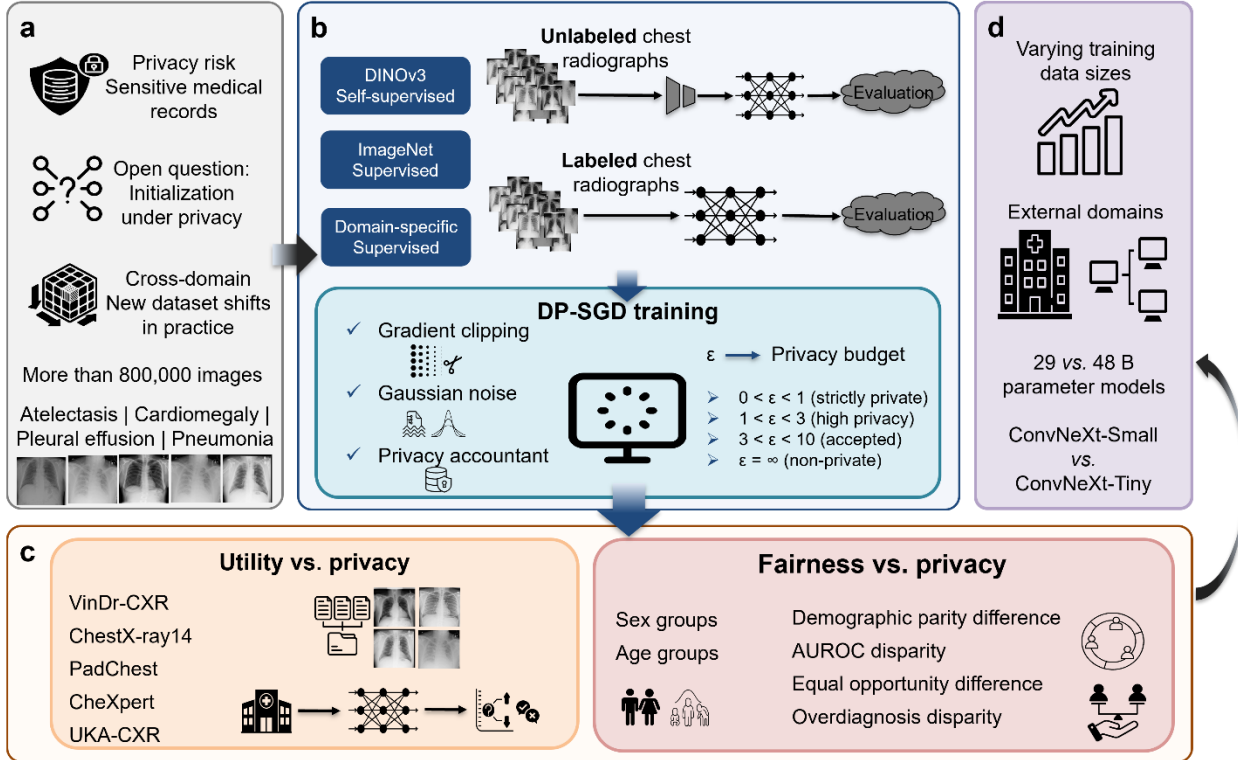


Figure 1: Study overview and experimental design. **a** Training deep learning models on sensitive medical images poses privacy risks, while real-world deployment requires robustness to cross-domain dataset shifts. The central open question addressed in this study is how model initialization influences utility, fairness, and generalization under differential privacy (DP). The study leverages a large and diverse collection of more than 800,000 chest radiographs aggregated from multiple datasets across different geographic regions (including the USA, Germany, Spain, and Vietnam), spanning standard and intensive care unit settings, multiple imaging protocols, labeling systems, and heterogeneous patient demographics. **b** ConvNeXt models are trained on chest radiographs using three initialization strategies: self-supervised DINOv3 pretraining on unlabeled images, supervised ImageNet pretraining, and domain-specific supervised pretraining on the largest publicly available chest radiograph dataset to date, MIMIC-CXR ($n = 213,921$), using the same five diagnostic labels as the downstream tasks: atelectasis, cardiomegaly, pleural effusion, pneumonia, and no finding. All models are trained end to end using DP-SGD across multiple privacy budgets, ranging from strict privacy ($0 < \epsilon < 1$) to non-private training ($\epsilon = \infty$). **c** Trained models are evaluated on five external chest radiograph datasets to quantify privacy-utility trade-offs and privacy-fairness trade-offs, including performance disparities across sex and age groups using multiple demographic fairness metrics. **d** To assess the robustness and generality of the main findings, a series of complementary generalization experiments is performed. These analyses evaluate whether the observed effects of initialization under DP depend on data scale, model capacity, or domain shift by examining cross-dataset generalization to external test sets, varying training set sizes, and comparing network architectures with different capacities, specifically ConvNeXt-Small (approximately 49 million parameters) and ConvNeXt-Tiny (approximately 28 million parameters).

Domain-specific supervised pretraining on MIMIC-CXR ($n = 170,153$ training radiographs) yielded the highest diagnostic utility under DP and consistently achieved performance closest to non-private models, while remaining statistically indistinguishable. For example, on VinDr-CXR, non-private training achieved an average AUROC of 92.8 ± 0.6 [91.5, 93.9], whereas domain-specific pretrained models reached 89.4 ± 0.7 [88.0, 90.7] under the most restrictive privacy range

($0 < \epsilon < 1$; $P < 0.001$) and improved to 91.4 ± 0.6 [90.1, 92.6] at larger privacy budgets ($3 < \epsilon < 10$), where the residual difference from non-private training was smaller but remained detectable ($P = 0.034$). Across PadChest, CheXpert, and UKA-CXR, domain-specific pretrained models remained within approximately 1.5 to 3.0 AUROC percentage points of their non-private counterparts, with all differences statistically significant ($P < 0.001$ for all comparisons). In contrast, models initialized with supervised ImageNet weights exhibited the largest and most persistent utility gaps under DP. On VinDr-CXR, ImageNet-initialized models achieved AUROC values of 71.4 ± 1.1 [69.2, 73.6], 75.2 ± 1.1 [72.9, 77.4], and 76.1 ± 1.1 [73.9, 78.0] across increasing privacy ranges, markedly below both the non-private baseline and domain-specific pretrained models. This pattern was consistent across all datasets and privacy ranges ($P < 0.001$ for all comparisons), indicating that generic natural-image pretraining is insufficient to stabilize optimization under DP for medical imaging tasks.

Table 1: Utility of differentially private ConvNeXt-Small models across datasets, privacy levels, and initialization strategies.

Model utility is evaluated using the area under the receiver operating characteristic curve (AUROC), accuracy, specificity, and sensitivity, each computed from 1,000 bootstrap resamples and averaged across five labels, including atelectasis, cardiomegaly, pleural effusion, pneumonia, and no finding. ConvNeXt-Small models were trained under three differential privacy (DP) regimes ($0 < \epsilon < 1$, $1 < \epsilon < 3$, and $3 < \epsilon < 10$) and compared against a non-private baseline ($\epsilon = \infty$). Results are reported for three initialization strategies: DINOv3, ImageNet, and domain-specific pretrained weights, based on MIMIC-CXR dataset ($n=213,921$). Performance is evaluated on five chest radiograph datasets: VinDr-CXR (training $n = 15,000$; test $n = 3,000$), ChestX-ray14 (training $n = 86,524$; test $n = 25,596$), PadChest (training $n = 88,480$; test $n = 22,045$), CheXpert (training $n = 128,355$; test $n = 29,321$), and UKA-CXR (training $n = 153,537$; test $n = 39,824$). Values are presented in percent as mean \pm standard deviation with corresponding 95% confidence intervals.

Initialization	Metric [%]	Epsilon	VinDr-CXR	ChestX-ray14	PadChest	CheXpert	UKA-CXR
DINOv3	AUROC	$0 < \epsilon < 1$	79.5 ± 1.2 [77.1, 81.8]	63.1 ± 0.3 [62.5, 63.8]	75.6 ± 0.3 [75.0, 76.1]	69.2 ± 0.3 [68.7, 69.8]	79.1 ± 0.2 [78.8, 79.4]
		$1 < \epsilon < 3$	80.4 ± 1.1 [78.0, 82.4]	64.6 ± 0.3 [63.9, 65.3]	75.9 ± 0.3 [75.4, 76.5]	69.6 ± 0.3 [69.1, 70.1]	80.1 ± 0.2 [79.8, 80.4]
		$3 < \epsilon < 10$	81.5 ± 1.0 [79.6, 83.4]	66.0 ± 0.3 [65.4, 66.7]	77.4 ± 0.3 [76.9, 77.9]	70.4 ± 0.3 [69.9, 70.9]	81.1 ± 0.2 [80.8, 81.4]
	Accuracy	$0 < \epsilon < 1$	77.0 ± 1.6 [73.7, 80.3]	54.8 ± 3.2 [48.6, 59.4]	70.2 ± 1.4 [67.3, 72.3]	69.1 ± 2.6 [60.9, 72.5]	71.7 ± 0.6 [70.4, 73.0]
		$1 < \epsilon < 3$	77.2 ± 1.1 [75.2, 79.2]	56.0 ± 4.3 [49.9, 62.3]	72.3 ± 2.2 [67.8, 75.6]	63.2 ± 4.2 [57.7, 73.7]	73.4 ± 0.7 [71.9, 74.8]
		$3 < \epsilon < 10$	75.9 ± 1.8 [72.4, 79.8]	60.5 ± 2.0 [56.2, 63.3]	66.5 ± 1.4 [64.0, 69.3]	71.0 ± 1.5 [67.7, 73.6]	74.5 ± 0.6 [73.5, 75.7]
	Specificity	$0 < \epsilon < 1$	75.5 ± 1.8 [71.9, 79.2]	55.7 ± 3.5 [48.8, 60.7]	69.9 ± 1.6 [66.6, 72.4]	69.0 ± 2.9 [60.2, 73.2]	71.3 ± 0.9 [69.5, 73.2]
		$1 < \epsilon < 3$	75.6 ± 1.4 [72.9, 78.3]	57.4 ± 4.7 [50.5, 64.4]	72.4 ± 2.5 [67.2, 76.2]	62.4 ± 4.4 [56.4, 73.7]	73.6 ± 1.1 [71.2, 75.7]
		$3 < \epsilon < 10$	74.9 ± 2.1 [71.0, 79.2]	61.7 ± 2.1 [57.0, 64.8]	66.3 ± 1.6 [63.4, 69.4]	70.8 ± 1.9 [66.9, 74.3]	74.7 ± 0.9 [73.1, 76.4]
	Sensitivity	$0 < \epsilon < 1$	74.5 ± 2.5 [69.4, 79.1]	65.3 ± 3.5 [60.0, 72.0]	71.6 ± 1.6 [69.2, 74.8]	61.6 ± 2.9 [57.3, 70.4]	73.5 ± 1.0 [71.6, 75.2]
		$1 < \epsilon < 3$	77.7 ± 2.1 [73.5, 81.5]	66.0 ± 4.6 [59.2, 72.8]	69.1 ± 2.5 [65.3, 74.1]	69.5 ± 4.5 [58.0, 75.2]	73.1 ± 1.1 [71.0, 75.4]
		$3 < \epsilon < 10$	78.1 ± 2.4 [73.0, 82.5]	63.7 ± 2.1 [60.3, 68.1]	77.0 ± 1.6 [73.6, 79.8]	62.3 ± 2.0 [58.6, 66.3]	73.7 ± 0.9 [71.9, 75.2]

Table 1: Continued.

Initialization	Metric [%]	Epsilon	VinDr-CXR	ChestX-ray14	PadChest	CheXpert	UKA-CXR	
ImageNet	AUROC	$0 < \epsilon < 1$	71.4 ± 1.1 [69.2, 73.6]	61.0 ± 0.4 [60.3, 61.7]	74.5 ± 0.3 [73.9, 75.1]	68.0 ± 0.2 [67.4, 68.5]	74.1 ± 0.2 [73.8, 74.5]	
		$1 < \epsilon < 3$	75.2 ± 1.1 [72.9, 77.4]	60.6 ± 0.3 [59.9, 61.3]	75.8 ± 0.3 [75.2, 76.3]	66.8 ± 0.3 [66.3, 67.3]	78.1 ± 0.2 [77.8, 78.4]	
		$3 < \epsilon < 10$	76.1 ± 1.1 [73.9, 78.0]	62.5 ± 0.3 [61.9, 63.2]	76.6 ± 0.3 [76.1, 77.2]	70.7 ± 0.2 [70.2, 71.2]	78.6 ± 0.2 [78.3, 78.9]	
	Accuracy	$0 < \epsilon < 1$	67.1 ± 2.5 [61.4, 70.9]	45.4 ± 2.6 [41.5, 50.6]	65.8 ± 1.5 [62.9, 68.8]	59.6 ± 5.9 [52.1, 71.7]	65.9 ± 0.8 [64.4, 67.6]	
		$1 < \epsilon < 3$	71.5 ± 2.0 [67.4, 74.9]	44.3 ± 2.0 [40.7, 49.4]	68.0 ± 0.9 [66.2, 69.7]	62.0 ± 4.5 [50.5, 69.2]	70.2 ± 0.7 [68.7, 71.3]	
		$3 < \epsilon < 10$	67.7 ± 3.4 [60.8, 73.2]	48.0 ± 1.3 [45.7, 50.4]	69.3 ± 1.8 [65.9, 72.1]	62.8 ± 2.6 [58.4, 69.0]	70.9 ± 0.6 [69.6, 72.1]	
	Specificity	$0 < \epsilon < 1$	66.7 ± 2.8 [60.2, 70.9]	44.5 ± 2.8 [40.0, 50.4]	64.9 ± 1.8 [61.5, 68.4]	57.4 ± 6.3 [49.0, 70.6]	64.2 ± 1.3 [61.4, 66.8]	
		$1 < \epsilon < 3$	70.6 ± 2.2 [66.1, 74.6]	42.4 ± 2.2 [38.3, 47.5]	67.3 ± 1.1 [65.2, 69.3]	59.8 ± 4.8 [47.7, 67.8]	69.0 ± 1.0 [66.9, 70.7]	
		$3 < \epsilon < 10$	67.7 ± 3.7 [60.1, 73.9]	47.1 ± 1.5 [44.3, 50.1]	68.7 ± 2.0 [64.9, 71.9]	60.7 ± 2.9 [55.8, 67.6]	69.5 ± 1.0 [67.4, 71.4]	
	Sensitivity	$0 < \epsilon < 1$	68.2 ± 2.8 [63.1, 73.9]	73.3 ± 2.8 [67.6, 77.6]	74.7 ± 1.8 [71.1, 78.0]	71.2 ± 6.4 [57.8, 79.5]	71.7 ± 1.3 [69.0, 74.5]	
		$1 < \epsilon < 3$	70.3 ± 2.5 [65.2, 75.2]	76.1 ± 2.2 [70.9, 80.0]	75.2 ± 1.1 [73.1, 77.4]	66.7 ± 4.8 [58.5, 78.5]	73.3 ± 1.0 [71.5, 75.3]	
		$3 < \epsilon < 10$	73.5 ± 3.6 [66.6, 80.5]	73.6 ± 1.5 [70.8, 76.5]	74.9 ± 2.0 [71.6, 78.8]	71.6 ± 3.0 [64.6, 76.3]	74.3 ± 1.0 [72.3, 76.4]	
Domain-specific	AUROC	$0 < \epsilon < 1$	89.4 ± 0.7 [88.0, 90.7]	74.4 ± 0.3 [73.7, 75.0]	83.9 ± 0.2 [83.4, 84.3]	77.1 ± 0.2 [76.6, 77.6]	84.4 ± 0.1 [84.2, 84.7]	
		$1 < \epsilon < 3$	91.5 ± 0.7 [90.0, 92.8]	74.7 ± 0.3 [74.0, 75.3]	84.2 ± 0.2 [83.8, 84.7]	77.2 ± 0.2 [76.7, 77.6]	84.8 ± 0.1 [84.5, 85.1]	
		$3 < \epsilon < 10$	91.4 ± 0.6 [90.1, 92.6]	75.0 ± 0.3 [74.4, 75.6]	85.8 ± 0.2 [85.3, 86.2]	77.2 ± 0.2 [76.7, 77.6]	85.3 ± 0.1 [85.0, 85.6]	
	Accuracy	$0 < \epsilon < 1$	87.2 ± 1.3 [84.6, 89.2]	69.4 ± 1.0 [67.3, 71.8]	78.5 ± 0.8 [77.1, 80.2]	71.7 ± 1.7 [68.3, 74.1]	77.3 ± 0.6 [76.0, 78.3]	
		$1 < \epsilon < 3$	87.4 ± 1.0 [85.4, 89.2]	69.3 ± 0.6 [68.1, 70.5]	76.6 ± 1.0 [74.6, 78.5]	71.7 ± 2.3 [67.6, 75.8]	76.7 ± 0.6 [75.5, 78.0]	
		$3 < \epsilon < 10$	86.6 ± 1.1 [84.7, 88.8]	68.2 ± 1.2 [65.9, 70.4]	80.1 ± 0.6 [78.9, 81.2]	71.5 ± 1.9 [67.2, 74.2]	78.4 ± 0.5 [77.4, 79.4]	
	Specificity	$0 < \epsilon < 1$	85.8 ± 1.4 [82.8, 88.2]	71.2 ± 1.3 [68.7, 73.8]	78.6 ± 1.1 [76.7, 80.7]	71.0 ± 1.9 [67.0, 73.9]	77.3 ± 0.9 [75.5, 79.0]	
		$1 < \epsilon < 3$	86.9 ± 1.1 [84.6, 88.9]	70.8 ± 0.9 [69.3, 72.6]	75.9 ± 1.1 [73.6, 78.1]	71.2 ± 2.6 [66.6, 75.9]	76.3 ± 0.8 [74.7, 78.2]	
		$3 < \epsilon < 10$	86.2 ± 1.3 [83.7, 88.8]	70.1 ± 1.4 [67.4, 72.7]	80.2 ± 0.7 [78.7, 81.5]	70.6 ± 2.1 [65.8, 73.9]	79.1 ± 0.7 [77.6, 80.5]	
	Sensitivity	$0 < \epsilon < 1$	82.6 ± 1.6 [79.5, 85.7]	66.7 ± 1.4 [63.9, 69.3]	76.9 ± 1.1 [74.6, 79.0]	71.5 ± 1.9 [68.5, 75.5]	76.7 ± 0.9 [75.0, 78.4]	
		$1 < \epsilon < 3$	85.8 ± 1.4 [82.9, 88.5]	68.4 ± 1.0 [66.2, 70.2]	79.5 ± 1.2 [77.1, 81.8]	71.2 ± 2.6 [66.6, 75.6]	78.2 ± 0.8 [76.3, 79.8]	
		$3 < \epsilon < 10$	85.5 ± 1.6 [82.3, 88.6]	68.9 ± 1.4 [66.0, 71.5]	79.0 ± 0.8 [77.5, 80.5]	72.1 ± 2.1 [68.7, 76.7]	76.5 ± 0.8 [74.9, 77.9]	
Non-DP								
Non-DP	AUROC	$\epsilon = \infty$	92.8 ± 0.6 [91.5, 93.9]	77.7 ± 0.3 [77.1, 78.2]	89.5 ± 0.2 [89.1, 89.9]	82.3 ± 0.2 [81.8, 82.7]	88.8 ± 0.1 [88.6, 89.0]	
			88.1 ± 1.0 [86.1, 89.9]	71.6 ± 1.4 [68.2, 73.6]	81.6 ± 0.6 [80.5, 82.8]	73.8 ± 1.2 [71.5, 76.1]	79.5 ± 0.3 [78.9, 80.1]	
	Accuracy		88.0 ± 1.1 [85.7, 90.1]	73.0 ± 1.6 [69.3, 75.6]	81.1 ± 0.7 [79.7, 82.5]	72.6 ± 1.4 [69.9, 75.4]	78.9 ± 0.6 [77.5, 80.0]	
			86.7 ± 1.4 [84.0, 89.3]	70.0 ± 1.6 [67.2, 73.6]	84.1 ± 0.8 [82.6, 85.7]	78.3 ± 1.4 [75.5, 80.8]	82.2 ± 0.6 [81.0, 83.5]	

Self-supervised DINOv3 initialization significantly improved diagnostic performance relative to ImageNet initialization across the majority of dataset and privacy combinations. Specifically, DINOv3 outperformed ImageNet in 13 out of 15 comparisons ($P \leq 0.012$), with two exceptions where differences were not statistically significant: CheXpert at $3 < \epsilon < 10$ ($P = 0.19$) and PadChest at $1 < \epsilon < 3$ ($P = 0.24$). For example, on PadChest, DINOv3-initialized models achieved AUROC values of 75.6 ± 0.3 [75.0, 76.1] at $0 < \epsilon < 1$ and 77.4 ± 0.3 [76.9, 77.9] at $3 < \epsilon < 10$, compared with 74.5 ± 0.3 [73.9, 75.1] ($P < 0.001$) and 76.6 ± 0.3 [76.1, 77.2] ($P = 0.0012$), respectively, for ImageNet initialization. Despite these gains, DINOv3 did not achieve non-private performance and remained consistently inferior to domain-specific supervised pretraining. On CheXpert, DINOv3 reached an AUROC of 70.4 ± 0.3 [69.9, 70.9] at higher privacy budgets, compared with 77.2 ± 0.2 [76.7, 77.6] for domain-specific pretraining and 82.3 ± 0.2 [81.8, 82.7] for non-private training ($P < 0.001$).

Across all initialization strategies and datasets, AUROC increased monotonically with increasing privacy budget in 29 out of 30 comparisons. The sole exception was ImageNet initialization on ChestX-ray14, where AUROC marginally decreased from 61.0 ± 0.4 [60.3, 61.7] at $0 < \epsilon < 1$ to 60.6 ± 0.3 [59.9, 61.3] at $1 < \epsilon < 3$ ($P = 0.55$). Overall, these results indicate a stable and interpretable privacy-utility trade-off rather than abrupt performance collapse. Importantly, the relative ordering of initialization strategies was preserved across privacy ranges and datasets. While self-supervised initialization represents a substantial advance over generic supervised pretraining for differentially private medical imaging, large-scale, task-aligned supervised pretraining remains the most effective strategy for achieving diagnostic utility approaching non-private models.

2.2. Initialization-dependent fairness effects under DP

We next examined how DP influences demographic fairness across sex and age, and how these effects depend on model initialization. Fairness was assessed using three complementary disparity metrics capturing distinct clinical failure modes: AUROC disparity, reflecting differences in discriminatory performance; equal opportunity difference (EOD), reflecting disparities in sensitivity; overdiagnosis disparity (OD), reflecting differences in false positive rates; and parity difference (PtD), reflecting signed differences in overall prediction accuracy between demographic groups, which is inherently influenced by subgroup-specific label prevalence and therefore interpreted alongside prevalence-independent metrics. Analyses were conducted independently for each dataset, initialization strategy, and privacy range using identical held-out test sets (**Table 2**, **Figure 3**), with underlying demographic distributions summarized in **Table 3**.

Across all datasets, sex-based disparities remained small in absolute magnitude, both in non-private and differentially private settings. In the non-private baseline, sex-based AUROC disparity ranged from 0.3 to 1.2 across datasets. Introducing DP did not fundamentally alter this pattern, although variability increased for some initialization strategies and privacy ranges. Comparing initialization strategies, DINOv3 and ImageNet exhibited similar ranges of sex-based AUROC disparity, generally remaining within the low single-digit range. For example, on VinDr-

CXR, sex-based AUROC disparity increased from 1.0 in the non-private model to 2.3 for DINOv3 and 3.4 for ImageNet at $1 < \epsilon < 3$, and further to 4.3 for DINOv3 at $3 < \epsilon < 10$. In contrast, domain-specific initialization consistently yielded smaller sex-based AUROC disparities, remaining at or below non-private levels on several datasets, including VinDr-CXR (0.3–0.9 under DP vs. 1.0 non-private) and UKA-CXR (0.2–0.5 under DP vs. 0.3 non-private). These results indicate that sex-based discriminatory performance is largely preserved under DP, with domain-specific pretraining providing the most stable behavior.

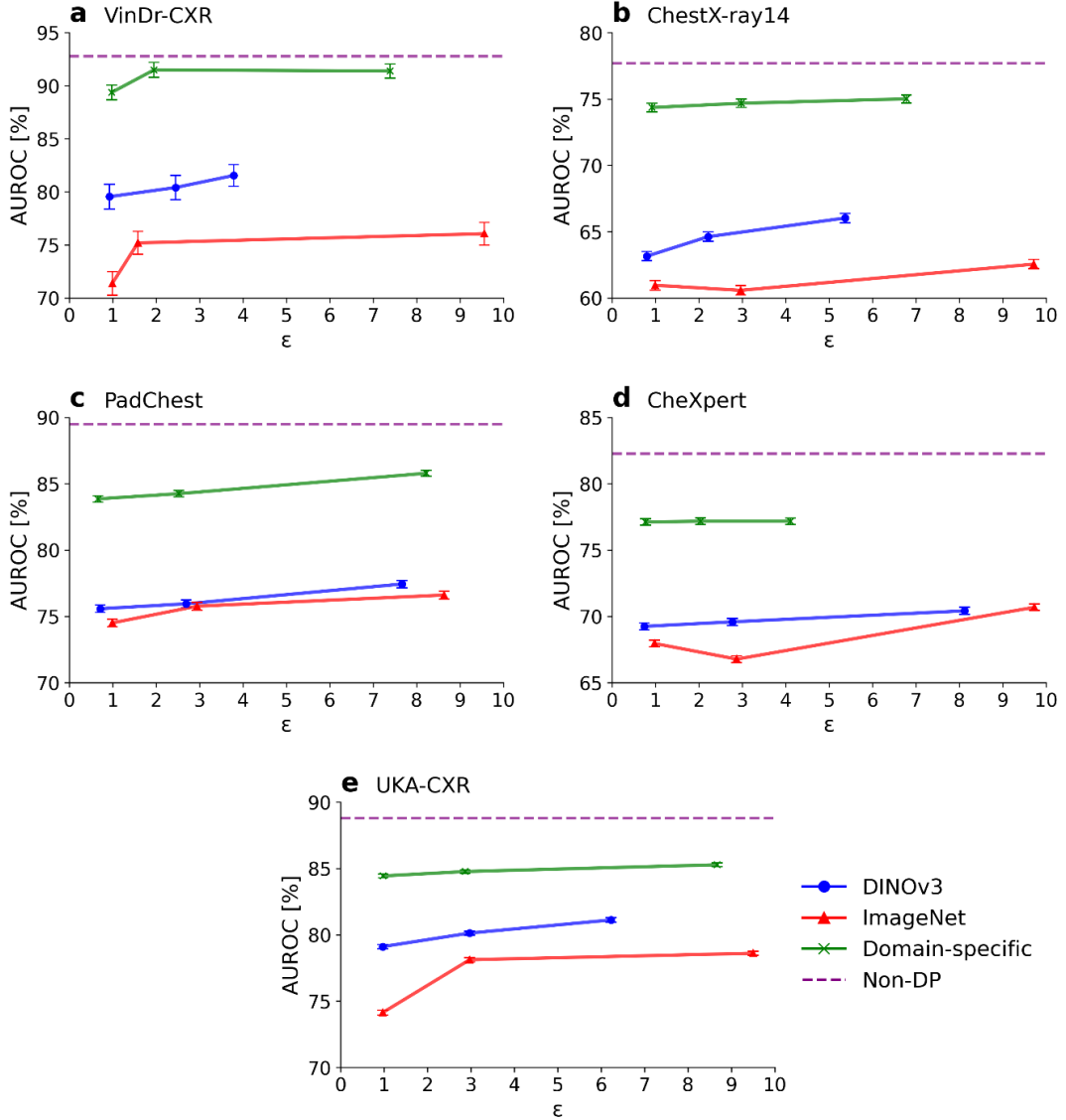


Figure 2: Diagnostic utility under DP across chest radiograph datasets. Label-averaged, across five labels, including atelectasis, cardiomegaly, pleural effusion, pneumonia, and no finding, AUROC values are shown for ConvNeXt-Small models evaluated on (a) VinDr-CXR (training n = 15,000; test n = 3,000), (b) ChestX-ray14 (training n = 86,524; test n = 25,596), (c) PadChest (training n = 88,480; test n = 22,045), (d) CheXpert (training n = 128,355; test n = 29,321), and (e) UKA-CXR (training n = 153,537; test n = 39,824). Each panel reports performance under non-private training (purple dashed line) and under differentially private training for three initialization strategies: self-supervised DINOv3 (blue circles), supervised ImageNet (red triangles), and domain-specific supervised pretraining on MIMIC-CXR (green markers). Privacy budgets (ϵ) are shown on the x-axis using the achieved ϵ values for each trained model, which may differ across datasets and initialization strategies due to dataset-specific convergence behavior. Error bars indicate variability across 1,000 bootstrap resamples.

Table 2: Fairness evaluation of differentially private ConvNeXt-Small models across datasets, privacy levels, and initialization strategies. Fairness is assessed separately across sex and age subgroups using three complementary metrics: AUROC disparity, equal opportunity difference (EOD), and overdiagnosis disparity (OD). AUROC disparity is defined as the absolute difference in subgroup AUROC values. EOD measures the absolute difference in true positive rates (sensitivity) between subgroups, reflecting disparities in disease detection. OD quantifies the absolute difference in false positive rates between subgroups and is computed from subgroup specificities. Results are reported for three initialization regimes (DINOv3, ImageNet, and domain-specific) and four privacy settings ($\epsilon = \infty$, $0 < \epsilon < 1$, $1 < \epsilon < 3$, and $3 < \epsilon < 10$). Metrics were computed from 1,000 bootstrap resamples and averaged across five labels, including atelectasis, cardiomegaly, pleural effusion, pneumonia, and no finding. Results are shown for five chest radiograph datasets: VinDr-CXR (training n = 15,000; test n = 3,000), ChestX-ray14 (training n = 86,524; test n = 25,596), PadChest (training n = 88,480; test n = 22,045), CheXpert (training n = 128,355; test n = 29,321), and UKA-CXR (training n = 153,537; test n = 39,824). Values are presented in percent.

Initialization	Metric [%]	Epsilon	VinDr-CXR		ChestX-ray14		PadChest		CheXpert		UKA-CXR	
			Sex	Age	Sex	Age	Sex	Age	Sex	Age	Sex	Age
DINOv3	AUROC disparity	$0 < \epsilon < 1$	1.0	6.0	0.1	6.5	2.1	9.0	1.0	4.3	0.9	3.5
		$1 < \epsilon < 3$	2.3	7.2	0.4	7.7	2.9	9.4	0.5	5.6	0.6	2.7
		$3 < \epsilon < 10$	4.3	7.9	0.6	7.0	0.5	8.2	0.5	4.6	0.6	2.5
	EOD	$0 < \epsilon < 1$	0.4	29.8	3.4	6.4	2.3	14.3	2.8	12.4	0.5	1.9
		$1 < \epsilon < 3$	10.2	23.8	7.7	13.0	3.0	16.8	2.3	3.5	2.3	1.6
		$3 < \epsilon < 10$	3.9	34.2	5.8	6.0	1.2	19.5	4.0	3.9	0.2	2.7
	OD	$0 < \epsilon < 1$	0.9	10.8	3.7	1.8	0.6	2.7	2.1	1.5	2.4	4.0
		$1 < \epsilon < 3$	7.1	22.5	7.1	2.3	1.9	2.9	2.4	7.7	3.4	5.4
		$3 < \epsilon < 10$	2.0	11.8	4.9	1.1	2.0	1.1	3.7	5.7	1.0	2.9
ImageNet	AUROC disparity	$0 < \epsilon < 1$	2.0	6.0	1.3	4.3	0.9	7.2	1.3	6.6	0.6	2.3
		$1 < \epsilon < 3$	3.4	6.9	0.7	4.6	0.2	7.0	1.1	7.3	0.5	2.9
		$3 < \epsilon < 10$	1.3	12.2	0.0	4.8	0.6	7.4	0.4	7.0	0.7	3.7
	EOD	$0 < \epsilon < 1$	2.9	37.1	4.5	11.1	3.4	1.8	0.9	7.5	0.9	1.3
		$1 < \epsilon < 3$	12.2	27.7	5.0	15.6	2.9	0.2	6.7	11.9	0.5	2.5
		$3 < \epsilon < 10$	5.1	24.2	1.0	11.0	3.3	5.1	0.8	15.1	1.0	0.9
	OD	$0 < \epsilon < 1$	0.3	6.1	3.3	1.9	4.1	16.7	0.0	6.6	0.6	6.7
		$1 < \epsilon < 3$	5.7	9.9	3.4	4.3	3.4	14.9	7.3	1.1	0.9	4.8
		$3 < \epsilon < 10$	2.8	12.7	2.1	4.9	3.4	8.8	0.5	2.6	0.5	6.5
Domain-specific	AUROC disparity	$0 < \epsilon < 1$	0.3	1.1	2.0	4.6	0.7	4.6	0.7	6.6	0.3	3.5
		$1 < \epsilon < 3$	0.9	1.4	2.5	4.0	0.2	3.8	1.1	6.8	0.2	3.7
		$3 < \epsilon < 10$	0.1	2.5	1.8	5.9	0.6	4.5	1.0	6.9	0.5	3.6
	EOD	$0 < \epsilon < 1$	6.2	30.7	3.5	7.2	4.3	0.8	3.2	9.5	1.2	3.8
		$1 < \epsilon < 3$	3.8	31.2	2.8	6.7	0.6	0.6	1.9	7.9	0.1	2.4
		$3 < \epsilon < 10$	0.6	30.0	1.8	4.3	0.2	0.5	1.5	10.6	0.9	1.7
	OD	$0 < \epsilon < 1$	2.5	6.1	0.2	3.2	3.9	8.9	4.5	3.4	0.4	3.8
		$1 < \epsilon < 3$	6.7	4.6	1.1	3.4	1.3	9.8	3.5	5.1	0.2	4.6
		$3 < \epsilon < 10$	2.4	2.9	1.3	3.5	2.6	8.9	2.8	3.6	1.9	4.8
Non-DP												
Non-DP	AUROC disparity	$\epsilon = \infty$	1.0	1.6	1.2	5.3	0.7	3.3	0.3	5.1	0.3	4.0
	EOD	$\epsilon = \infty$	0.2	29.0	1.7	1.4	2.4	0.1	2.7	6.8	0.7	3.7
	OD	$\epsilon = \infty$	3.3	6.4	0.2	6.5	0.0	6.4	3.1	3.4	0.2	5.3

Threshold-dependent fairness metrics revealed clearer differences between initialization strategies. In the non-private setting, sex-based EOD and OD were low across datasets, with EOD between 0.2 and 2.7 and OD between 0.0 and 3.3. Under DP, both DINOv3 and ImageNet showed pronounced increases in variability, particularly at intermediate privacy levels. On VinDr-CXR at $1 < \epsilon < 3$, sex-based EOD rose to 10.2 for DINOv3 and 12.2 for ImageNet, compared with 0.2 in the non-private baseline. Similar fluctuations were observed on ChestX-ray14 and

PadChest. These deviations did not follow a consistent direction across datasets or privacy levels, suggesting sensitivity to optimization noise and dataset structure rather than a systematic sex-related bias. By contrast, domain-specific initialization substantially constrained threshold-dependent disparities, with sex-based EOD remaining ≤ 3.8 on VinDr-CXR and ≤ 1.2 on UKA-CXR across privacy ranges, closely matching non-private behavior.

Table 3: Demographic composition of the test cohorts across chest radiograph datasets. The table reports the distribution of test-set images stratified by demographic group and diagnostic label for VinDr-CXR, ChestX-ray14, PadChest, CheXpert, and UKA-CXR. For each dataset, the total number of test images is shown separately for female and male patients, as well as for three age groups (<40 years, 40–70 years, and >70 years). Within each demographic subgroup, image counts are further broken down by label, where counts correspond to images in which the respective finding is present.

Demographic group	Images [n (%)]	VinDr-CXR	ChestX-ray14	PadChest	CheXpert	UKA-CXR
Full test set	Total images	3,000 (100%)	25,596 (100%)	22,045 (100%)	29,321 (100%)	39,824 (100%)
	Atelectasis	86 (3%)	3,279 (13%)	1,240 (6%)	4,523 (15%)	5,575 (14%)
	Cardiomegaly	309 (10%)	1,069 (4%)	1,954 (9%)	3,944 (13%)	18,616 (47%)
	Pleural effusion	111 (4%)	4,658 (18%)	1,373 (6%)	11,438 (39%)	5,049 (13%)
	Pneumonia	246 (8%)	555 (2%)	992 (4%)	816 (3%)	5,844 (15%)
	No finding	2,051 (68%)	9,861 (39%)	7,216 (33%)	3,540 (12%)	15,273 (38%)
Female	Total images	552 (100%)	10,714 (100%)	10,636 (100%)	11,436 (100%)	14,457 (100%)
	Atelectasis	18 (3%)	1,363 (13%)	529 (5%)	1,670 (15%)	1,931 (13%)
	Cardiomegaly	124 (22%)	528 (5%)	1,050 (10%)	1,541 (13%)	5,748 (40%)
	Pleural effusion	23 (4%)	1,921 (18%)	504 (5%)	4,520 (40%)	1,828 (13%)
	Pneumonia	37 (7%)	221 (2%)	426 (4%)	307 (3%)	1,846 (13%)
	No finding	308 (56%)	4,151 (39%)	4,083 (38%)	1,422 (12%)	6,408 (44%)
Male	Total images	702 (100%)	14,882 (100%)	11,408 (100%)	17,885 (100%)	25,367 (100%)
	Atelectasis	29 (4%)	1,916 (13%)	711 (6%)	2,853 (16%)	3,644 (14%)
	Cardiomegaly	58 (8%)	541 (4%)	904 (8%)	2,403 (13%)	12,868 (51%)
	Pleural effusion	43 (6%)	2,737 (18%)	869 (8%)	6,918 (39%)	3,221 (13%)
	Pneumonia	77 (11%)	334 (2%)	566 (5%)	509 (3%)	3,998 (16%)
	No finding	392 (56%)	5,710 (38%)	3,133 (27%)	2,118 (12%)	8,865 (35%)
Age below 40 years	Total images	2,681 (100%)	8,411 (100%)	3,748 (100%)	4,391 (100%)	2,297 (100%)
	Atelectasis	69 (3%)	801 (10%)	93 (2%)	488 (11%)	333 (14%)
	Cardiomegaly	240 (9%)	415 (5%)	39 (1%)	460 (10%)	639 (28%)
	Pleural effusion	96 (4%)	1,336 (16%)	101 (3%)	1,188 (27%)	228 (10%)
	Pneumonia	211 (8%)	229 (3%)	302 (8%)	131 (3%)	387 (17%)
	No finding	1,932 (72%)	3,489 (41%)	2,191 (58%)	1,018 (23%)	1,161 (51%)
Age between 40 and 70 years	Total images	250 (100%)	15,495 (100%)	10,788 (100%)	16,421 (100%)	19,197 (100%)
	Atelectasis	14 (6%)	2,157 (14%)	546 (5%)	2,648 (16%)	2,702 (14%)
	Cardiomegaly	37 (15%)	575 (4%)	560 (5%)	1,955 (12%)	8,262 (43%)
	Pleural effusion	11 (4%)	2,884 (19%)	491 (5%)	6,288 (38%)	2,269 (12%)
	Pneumonia	26 (10%)	305 (2%)	331 (3%)	394 (2%)	3,041 (16%)
	No finding	115 (46%)	5,782 (37%)	4,081 (38%)	2,036 (12%)	7,864 (41%)
Age above 70 years	Total images	69 (100%)	1,690 (100%)	7,503 (100%)	8,509 (100%)	18,328 (100%)
	Atelectasis	3 (4%)	321 (19%)	601 (8%)	1,387 (16%)	2,539 (14%)
	Cardiomegaly	32 (46%)	79 (5%)	1,354 (18%)	1,529 (18%)	9,713 (53%)
	Pleural effusion	4 (6%)	438 (26%)	780 (10%)	3,962 (47%)	2,552 (14%)
	Pneumonia	9 (13%)	21 (1%)	359 (5%)	291 (3%)	2,415 (13%)
	No finding	4 (6%)	590 (35%)	942 (13%)	486 (6%)	6,248 (34%)

Age-based disparities were substantially larger than sex-based disparities across all metrics and were already evident in non-private models. In the non-private setting, age-based AUROC disparity reached 5.3 on ChestX-ray14 and 5.1 on CheXpert, compared with 1.6 on VinDr-CXR. Under DP, age-based AUROC disparity increased across all initialization strategies, but the magnitude of this increase depended strongly on initialization. ImageNet initialization consistently exhibited the largest age-based AUROC disparities, reaching up to 12.2 on VinDr-CXR at $3 < \epsilon < 10$. DINOv3 reduced age-based AUROC disparity relative to ImageNet across most datasets and privacy ranges, for example yielding 7.9 on VinDr-CXR at $3 < \epsilon < 10$ compared with 12.2 for ImageNet, but disparities remained elevated relative to non-private baselines. Domain-specific initialization provided the strongest mitigation, particularly on VinDr-CXR, where age-based AUROC disparity remained between 1.1 and 2.5 under DP, compared with 1.6 in the non-private model.

Age-based EOD exposed the largest sensitivity gaps observed in the study and showed strong dataset dependence. On VinDr-CXR, age-based EOD was already high in the non-private model (29.0) and remained similarly elevated under DP for all initialization strategies, reaching up to 34.2 for DINOv3. In contrast, on PadChest and UKA-CXR, non-private age-based EOD was low (0.1 and 3.7, respectively). Under DP, domain-specific initialization preserved these low sensitivity gaps, remaining ≤ 0.8 on PadChest and ≤ 3.8 on UKA-CXR, whereas DINOv3 and ImageNet exhibited substantially larger age-based EOD on PadChest, reaching 19.5 and 5.1, respectively. These findings indicate that DP does not introduce age-related sensitivity disparities where none exist, but can markedly amplify pre-existing imbalances when initialization is less task-aligned. A similar pattern was observed for age-based OD. In the non-private setting, age-based OD ranged from 3.4 to 6.5 across datasets. Under DP, ImageNet initialization showed the largest increases, most notably on PadChest, where age-based OD reached 16.7 at $0 < \epsilon < 1$. DINOv3 reduced but did not eliminate these increases, while domain-specific initialization consistently limited age-based OD, for example on VinDr-CXR (2.9–6.1 under DP vs. 6.4 non-private) and ChestX-ray14 (approximately 3.2–3.5 under DP vs. 6.5 non-private).

These results show that the demographic fairness under DP is strongly modulated by initialization strategy rather than privacy alone. Sex-based disparities remain small across all settings, while age-based disparities are larger and largely reflect dataset-specific characteristics already present in non-private models. Compared with ImageNet initialization, DINOv3 consistently improves fairness under DP, particularly for age-based discrimination and overdiagnosis, but does not fully stabilize threshold-dependent disparities. Domain-specific supervised pretraining provides the most consistent alignment with non-private fairness profiles, demonstrating that initialization choice is a critical determinant of fairness-privacy trade-offs in differentially private chest radiograph classification.

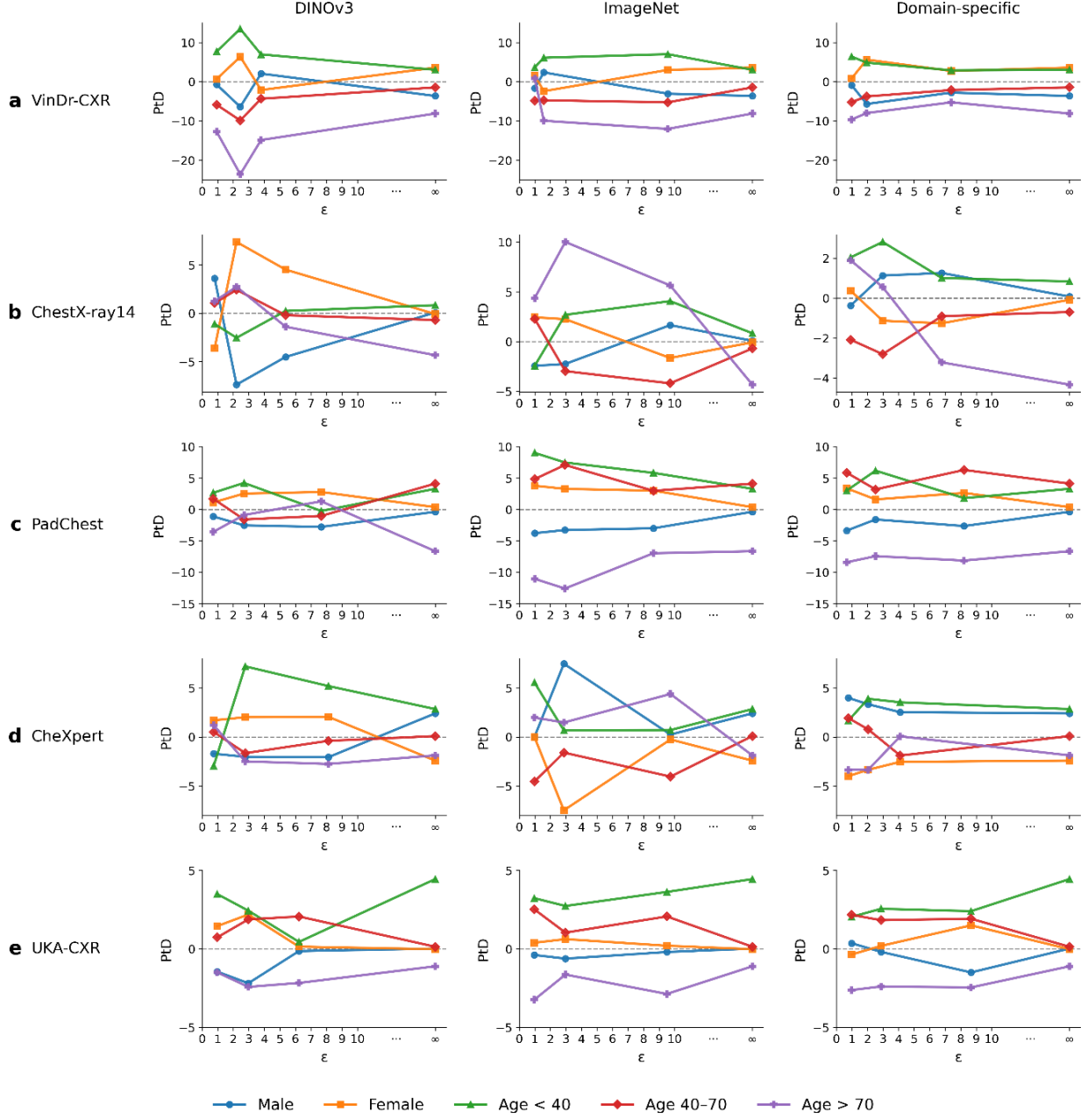


Figure 3: Demographic fairness under DP across chest radiograph datasets and initialization strategies. Statistical parity difference (PtD) is shown as a function of the privacy budget (ϵ) for ConvNeXt-Small models evaluated on (a) VinDr-CXR (training $n = 15,000$; test $n = 3,000$), (b) ChestX-ray14 (training $n = 86,524$; test $n = 25,596$), (c) PadChest (training $n = 88,480$; test $n = 22,045$), (d) CheXpert (training $n = 128,355$; test $n = 29,321$), and (e) UKA-CXR (training $n = 153,537$; test $n = 39,824$). Columns correspond to initialization strategy: self-supervised DINOv3 (left), supervised ImageNet (middle), and domain-specific supervised pretraining on MIMIC-CXR (right). Within each panel, separate curves report PtD for sex subgroups (male, female) and age subgroups (age < 40 years, age 40 to 70 years, and age > 70 years). Results are shown for differentially private models across the achieved privacy budgets and for the non-private baseline ($\epsilon = \infty$). Privacy budgets correspond to the final ϵ attained by each trained model and may differ across datasets and initialization strategies due to dataset-specific convergence behavior. PtD values are averaged across five diagnostic labels. Demographic composition of the test cohorts underlying these analyses is summarized in **Table 3**.

2.3. Initialization-dependent cross-dataset generalization under differential privacy

Cross-dataset generalization was used to assess whether the advantages conferred by strong initialization under DP extend beyond in-domain evaluation. ConvNeXt-Small models were trained on a combined cohort comprising all five datasets (total training $n = 471,896$ images) and evaluated independently on each dataset. This setting exposes models to substantial heterogeneity during training while testing their ability to generalize to institution-specific data under privacy constraints (**Table 4, Figure 4**).

Table 4: Domain generalization of differentially private ConvNeXt-Small models across initialization strategies and privacy levels. ConvNeXt-Small models are trained on the combined chest radiograph cohort from five datasets (total training $n = 471,896$ images) and evaluated on each dataset independently to measure cross domain generalization under differential privacy. The table reports AUROC values (mean \pm standard deviation from 1,000 bootstrap resamples), averaged across five labels, including atelectasis, cardiomegaly, pleural effusion, pneumonia, and no finding, together with changes relative to the corresponding non private baseline for each initialization strategy (Δ -AUROC). Results are shown for DINOv3, ImageNet, and domain-specific initializations across four privacy settings ($\epsilon = \infty$, $0 < \epsilon < 1$, $1 < \epsilon < 3$, and $3 < \epsilon < 10$). External evaluation datasets include VinDr-CXR (test $n = 3,000$), ChestX-ray14 (test $n = 25,596$), PadChest (test $n = 22,045$), CheXpert (test $n = 29,321$), and UKA-CXR (test $n = 39,824$). Values are presented in percent.

Initialization	Epsilon	Metric [%]	VinDr-CXR	ChestX-ray14	PadChest	CheXpert	UKA-CXR
DINOv3	0 < $\epsilon < 1$	AUROC	81.3 \pm 0.9	63.4 \pm 0.3	76.0 \pm 0.3	67.6 \pm 0.3	76.4 \pm 0.2
		Δ from non-DP	-12.1 \pm 0.5	-16.1 \pm 0.0	-14.1 \pm 0.1	-15.3 \pm 0.0	-12.4 \pm 0.0
	1 < $\epsilon < 3$	AUROC	79.9 \pm 1.0	61.9 \pm 0.3	75.7 \pm 0.3	67.5 \pm 0.3	76.6 \pm 0.2
		Δ from non-DP	-13.5 \pm 0.5	-17.7 \pm 0.1	-14.4 \pm 0.1	-15.4 \pm 0.0	-12.1 \pm 0.1
	3 < $\epsilon < 10$	AUROC	83.6 \pm 0.9	63.2 \pm 0.3	76.3 \pm 0.3	68.6 \pm 0.3	78.5 \pm 0.2
		Δ from non-DP	-9.8 \pm 0.4	-16.4 \pm 0.0	-13.7 \pm 0.1	-14.4 \pm 0.0	-10.3 \pm 0.0
ImageNet	0 < $\epsilon < 1$	AUROC	74.5 \pm 1.1	59.5 \pm 0.4	74.4 \pm 0.3	64.5 \pm 0.3	70.4 \pm 0.2
		Δ from non-DP	-18.9 \pm 0.7	-20.1 \pm 0.1	-15.7 \pm 0.1	-18.5 \pm 0.0	-18.4 \pm 0.1
	1 < $\epsilon < 3$	AUROC	77.6 \pm 1.0	61.1 \pm 0.3	75.0 \pm 0.3	65.0 \pm 0.3	71.9 \pm 0.2
		Δ from non-DP	-15.8 \pm 0.5	-18.5 \pm 0.1	-15.0 \pm 0.1	-18.0 \pm 0.0	-16.9 \pm 0.1
	3 < $\epsilon < 10$	AUROC	78.8 \pm 1.0	62.0 \pm 0.3	76.1 \pm 0.3	68.1 \pm 0.3	77.0 \pm 0.2
		Δ from non-DP	-14.6 \pm 0.6	-17.6 \pm 0.0	-14.0 \pm 0.1	-14.9 \pm 0.0	-11.7 \pm 0.1
Domain-specific	0 < $\epsilon < 1$	AUROC	89.5 \pm 0.6	71.3 \pm 0.3	81.9 \pm 0.3	76.1 \pm 0.3	82.0 \pm 0.1
		Δ from non-DP	-3.8 \pm 0.1	-8.3 \pm 0.0	-8.2 \pm 0.1	-6.8 \pm 0.0	-6.8 \pm 0.0
	1 < $\epsilon < 3$	AUROC	90.0 \pm 0.6	71.8 \pm 0.3	82.7 \pm 0.2	76.1 \pm 0.2	82.7 \pm 0.1
		Δ from non-DP	-3.4 \pm 0.2	-7.8 \pm 0.0	-7.3 \pm 0.1	-6.9 \pm 0.0	-6.1 \pm 0.0
	3 < $\epsilon < 10$	AUROC	90.8 \pm 0.6	71.8 \pm 0.3	82.7 \pm 0.2	75.4 \pm 0.2	82.6 \pm 0.1
		Δ from non-DP	-2.5 \pm 0.1	-7.8 \pm 0.0	-7.3 \pm 0.1	-7.6 \pm 0.0	-6.2 \pm 0.0
Non-DP	$\epsilon = \infty$	AUROC	93.4 \pm 0.5	79.6 \pm 0.3	90.1 \pm 0.2	83.0 \pm 0.2	88.8 \pm 0.1

Under non-private training, models trained on the combined cohort achieved high and stable AUROC across all evaluation datasets, ranging from 79.6 ± 0.3 on ChestX-ray14 to 93.4 ± 0.5 on VinDr-CXR. These results confirm that large-scale aggregation effectively supports cross-institutional generalization when privacy constraints are absent. Introducing DP consistently reduced AUROC across all datasets and initialization strategies, demonstrating that privacy noise impacts not only in-domain performance but also generalization across distribution shifts. Importantly, these reductions were observed despite training on data pooled from all evaluation domains, indicating that dataset aggregation alone does not eliminate privacy-induced generalization costs.

Initialization strategy again emerged as the dominant factor governing robustness under DP. Models initialized with supervised ImageNet weights exhibited the largest drops in AUROC relative to their non-private baselines across all datasets and privacy ranges. For example, at $0 < \epsilon < 1$, ImageNet-initialized models showed AUROC reductions of 19.0 on VinDr-CXR, 20.1 on ChestX-ray14, and 18.5 on CheXpert. Even at larger privacy budgets ($3 < \epsilon < 10$), substantial performance gaps persisted, with Δ AUROC values remaining between -11.7 and -17.6 across datasets.

Self-supervised DINOv3 initialization substantially improved cross-dataset generalization under DP relative to ImageNet initialization. Across datasets and privacy ranges, DINOv3 consistently yielded smaller AUROC reductions, with Δ AUROC values typically 3.0 to 7.0 lower than those observed for ImageNet ($P < 0.001$). For instance, at $0 < \epsilon < 1$, DINOv3 reduced the AUROC drop on VinDr-CXR from -18.9 (ImageNet) to -12.1, and on UKA-CXR from -18.4 to -12.4. Similar relative improvements were observed across ChestX-ray14, PadChest, and CheXpert. These results indicate that self-supervised representations improve resilience to privacy noise in the presence of cross-domain variation. Despite these gains, self-supervised initialization did not fully close the generalization gap to domain-specific supervised pretraining. Across all datasets and privacy levels, models initialized with supervised pretraining on large chest radiograph cohorts consistently exhibited the smallest AUROC reductions under DP. At $0 < \epsilon < 1$, domain-specific initialization limited Δ AUROC to -3.8 on VinDr-CXR and to between -6.8 and -8.3 on the remaining datasets. Even under the most permissive privacy range ($3 < \epsilon < 10$), residual gaps to non-private performance remained but were substantially smaller than for DINOv3 or ImageNet initialization, with Δ AUROC as low as -2.5 on VinDr-CXR and remaining below -7.6 on all other datasets.

Across all initialization strategies, increasing the privacy budget led to monotonic improvements in AUROC and reduced generalization gaps, but did not alter the relative ordering of initialization strategies. Domain-specific supervised pretraining consistently provided the strongest protection against privacy-induced degradation, followed by self-supervised DINOv3, with ImageNet initialization performing worst. Notably, even under the largest privacy budgets, a persistent gap between differentially private and non-private models remained across all datasets, underscoring that DP imposes a fundamental cost on cross-dataset generalization that is not fully mitigated by data scale alone. These results demonstrate that the role of initialization in differentially private training extends beyond in-domain performance to cross-dataset generalization. Self-supervised initialization substantially improves robustness under privacy

constraints compared with generic supervised pretraining, but remains inferior to task-aligned supervised initialization when large labeled medical datasets are available. This finding reinforces the central conclusion of the study: under DP, initialization choice is a key determinant of both diagnostic utility and cross-domain generalization, and domain-specific supervision remains the most effective strategy when accessible.

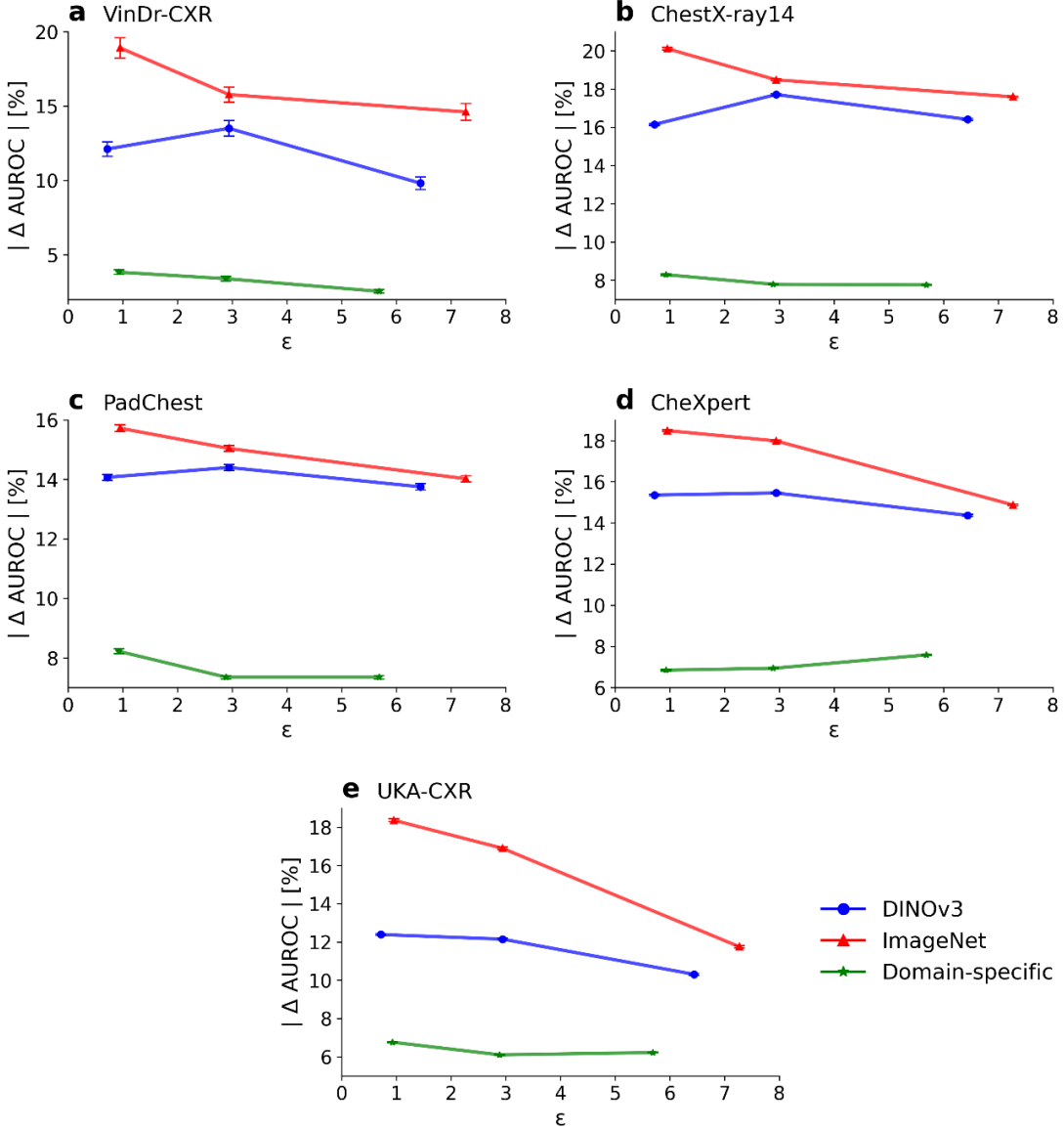


Figure 4: Cross-dataset generalization under DP. Absolute changes in diagnostic performance relative to the corresponding non-private baseline ($|\Delta \text{AUROC}|$) are shown for ConvNeXt-Small models trained on a combined multi-dataset cohort (total training $n = 471,897$) and evaluated independently on (a) VinDr-CXR (test $n = 3,000$), (b) ChestX-ray14 (test $n = 25,596$), (c) PadChest (test $n = 22,045$), (d) CheXpert (test $n = 29,321$), and (e) UKA-CXR (test $n = 39,824$). Curves are shown for three initialization strategies under differentially private training: self-supervised DINOv3 (blue circles), supervised ImageNet (red triangles), and domain-specific supervised pretraining on MIMIC-CXR (green markers). Privacy budgets (ϵ) are shown on the x-axis using the achieved ϵ values for each trained model, which may differ across datasets and initialization strategies due to dataset-specific convergence behavior. Values indicate the absolute magnitude of performance change relative to the non-private model, such that larger values correspond to larger generalization degradation under DP. Error bars indicate variability across 1,000 bootstrap resamples. AUROC values were averaged across five labels, including atelectasis, cardiomegaly, pleural effusion, pneumonia, and no finding.

2.4. Generalization across model capacity under DP

We varied model capacity to assess whether the effects of DP and initialization observed for ConvNeXt-Small persist when using a smaller architecture, ConvNeXt-Tiny (approximately 28 million parameters). Across all five datasets, ConvNeXt-Tiny exhibited slightly lower diagnostic performance than ConvNeXt-Small (approximately 49 million parameters) in the non-private setting, consistent with the expected reduction in representational capacity. Comparisons between architectures are shown in **Figure 5**, with detailed results for ConvNeXt-Tiny provided in **Supplementary Tables 1–3**. For example, under non-private training, average AUROC on VinDr-CXR decreased from 92.8 ± 0.6 [91.5, 93.9] with ConvNeXt-Small to 92.3 ± 0.7 [90.9, 93.5] with ConvNeXt-Tiny, and on PadChest from 89.5 ± 0.2 [89.1, 89.9] to 89.3 ± 0.2 [88.9, 89.7], indicating modest but systematic capacity-related differences. Under DP, the same pattern was largely preserved, with ConvNeXt-Tiny generally achieving lower AUROC than ConvNeXt-Small across privacy ranges and initialization strategies. Importantly, however, the relative ordering of initialization strategies remained unchanged across model sizes. For both architectures, domain-specific supervised pretraining on MIMIC-CXR consistently yielded the highest AUROC under DP, followed by self-supervised DINOv3 initialization and then supervised ImageNet initialization. This ordering held across all datasets and privacy regimes.

Under strong privacy constraints ($0 < \epsilon < 1$), the advantage of task-aligned pretraining remained pronounced for ConvNeXt-Tiny. On ChestX-ray14, ConvNeXt-Tiny achieved an AUROC of 74.9 ± 0.3 [74.2, 75.4] with domain-specific initialization, compared with 64.0 ± 0.3 [63.3, 64.7] for DINOv3 and 60.4 ± 0.3 [59.8, 61.1] for ImageNet ($P < 0.001$). Similar gaps were observed on PadChest, where domain-specific initialization reached 84.6 ± 0.2 [84.1, 85.1] under DP, compared with 75.2 ± 0.3 [74.6, 75.7] for DINOv3 and 75.3 ± 0.3 [74.7, 75.8] for ImageNet ($P < 0.001$). These differences closely mirrored those observed for ConvNeXt-Small, indicating that initialization effects are not attenuated by reduced model capacity. Across all initialization strategies and datasets for ConvNeXt-Tiny, AUROC increased monotonically with increasing privacy budget in 26 out of 30 comparisons, reflecting a stable privacy-utility trade-off. At larger privacy budgets ($3 < \epsilon < 10$), ConvNeXt-Tiny achieved AUROC values of 92.5 ± 0.6 [91.3, 93.6] on VinDr-CXR, 85.8 ± 0.2 [85.3, 86.2] on PadChest, and 85.5 ± 0.1 [85.2, 85.7] on UKA-CXR with domain-specific initialization. In comparison, DINOv3-initialized models reached 80.2 ± 1.0 [78.2, 82.1], 77.0 ± 0.3 [76.4, 77.5], and 81.8 ± 0.1 [81.5, 82.1] on the same datasets, while ImageNet-initialized models remained lower at 79.6 ± 1.0 [77.6, 81.5], 76.6 ± 0.3 [76.0, 77.1], and 81.7 ± 0.1 [81.4, 82.0], respectively. Although absolute performance remained below the non-private baseline ($P < 0.001$ for all comparisons), the relative gaps between initialization strategies were consistent with those observed for ConvNeXt-Small.

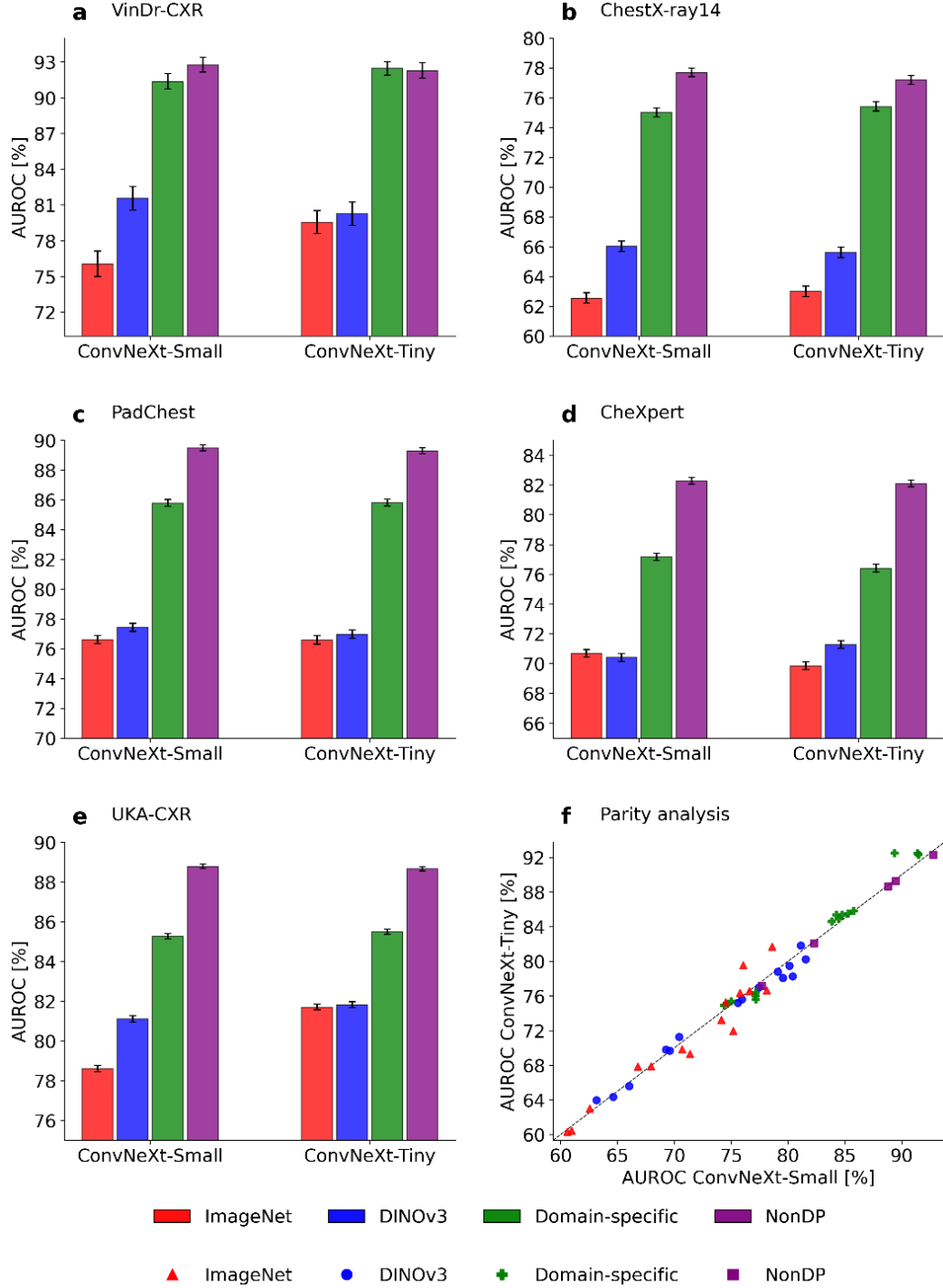


Figure 5: Generalization across model capacity under differential privacy. Average AUROC values, averaged across five labels, including atelectasis, cardiomegaly, pleural effusion, pneumonia, and no finding, are shown for ConvNeXt-Small (approximately 49 million parameters) and ConvNeXt-Tiny (approximately 28 million parameters) models evaluated on (a) VinDr-CXR (training n = 15,000; test n = 3,000), (b) ChestX-ray14 (training n = 86,524; test n = 25,596), (c) PadChest (training n = 88,480; test n = 22,045), (d) CheXpert (training n = 128,355; test n = 29,321), and (e) UKA-CXR (training n = 153,537; test n = 39,824). For each dataset, bar plots report values under non-private training and under DP training at the largest privacy range ($3 < \epsilon < 10$), shown separately for ImageNet, DINOv3, and domain-specific initialization. ConvNeXt-Small and ConvNeXt-Tiny results are displayed side by side to facilitate direct comparison across model capacities. Panel (f) shows a parity analysis comparing AUROC of ConvNeXt-Small (x-axis) and ConvNeXt-Tiny (y-axis) across datasets, privacy settings, and initialization strategies, with the diagonal indicating equal performance. Error bars indicate variability across 1,000 bootstrap resamples.

Notably, the absolute difference between ConvNeXt-Small and ConvNeXt-Tiny under DP was generally smaller than the difference induced by changing the initialization strategy. For example, under strong privacy on VinDr-CXR, switching from ImageNet to domain-specific initialization increased AUROC by more than 23 percentage points for ConvNeXt-Tiny (from 69.3 ± 1.2 [67.0, 71.6] to 92.5 ± 0.6 [91.3, 93.6]), far exceeding the sub-1 percentage point gap attributable to model capacity in the non-private setting. This pattern was consistent across datasets and privacy regimes. The effects of DP and initialization generalize robustly across model capacity. While reducing model size leads to modest decreases in absolute performance, initialization strategy exerts a substantially stronger and more consistent influence on diagnostic utility under DP than architectural capacity. The close correspondence between ConvNeXt-Small and ConvNeXt-Tiny across datasets and privacy levels indicates that the observed benefits of domain-specific and self-supervised initialization reflect stable properties of differentially private training, rather than idiosyncrasies of a particular model size.

2.5. Effect of training set size under differential privacy

Training set size had a substantial impact on diagnostic performance under DP on PadChest, which was selected as a representative large-scale chest radiograph dataset due to its broad pathology coverage and sufficient sample size to support controlled subsampling experiments (**Figure 6**). ConvNeXt-Small models were trained on progressively larger fractions of the PadChest training set, ranging from 10% to the full dataset, while evaluation was performed on a fixed held-out test cohort. This design isolates the interaction between data availability, privacy constraints, and initialization strategy, enabling systematic assessment of how privacy noise scales with dataset size in a setting that reflects realistic data availability constraints in medical imaging.

Across all privacy regimes and initialization strategies, diagnostic performance increased monotonically with training set size, indicating that additional data partially mitigates the performance degradation induced by DP. Under non-private training, AUROC improved from 84.3 ± 0.2 [83.9, 84.8] when using 10% of the training data ($n=8,821$) to 89.5 ± 0.2 [89.1, 89.9] ($P < 0.001$) when using the full dataset ($n=88,480$). Under DP, this dependence on dataset size was substantially more pronounced. For example, with self-supervised DINOv3 initialization under strong privacy constraints ($0 < \epsilon < 1$), AUROC increased from 64.6 ± 0.3 [64.1, 65.3] at 10% of the data to 75.6 ± 0.3 [75.0, 76.1] at full dataset size, corresponding to an absolute gain of nearly 11 percentage points. Initialization strategy exerted a consistent influence across all data fractions and privacy regimes. At most of the training set size examined, models initialized with self-supervised DINOv3 weights outperformed those initialized with supervised ImageNet weights. This advantage was most pronounced in low-data regimes under strong privacy constraints ($P < 0.001$ for all comparisons). At 10% of the training data and $0 < \epsilon < 1$, DINOv3 achieved an AUROC of 64.6 ± 0.3 [64.1, 65.3], compared with 62.7 ± 0.3 [62.1, 63.4] for ImageNet initialization. At 25% of the data ($n=22,160$), the gap widened to 72.7 ± 0.3 [72.1, 73.3] vs. 67.2 ± 0.3 [66.5, 67.8], indicating that self-supervised representations substantially improve robustness to the combined effects of data scarcity and privacy noise.

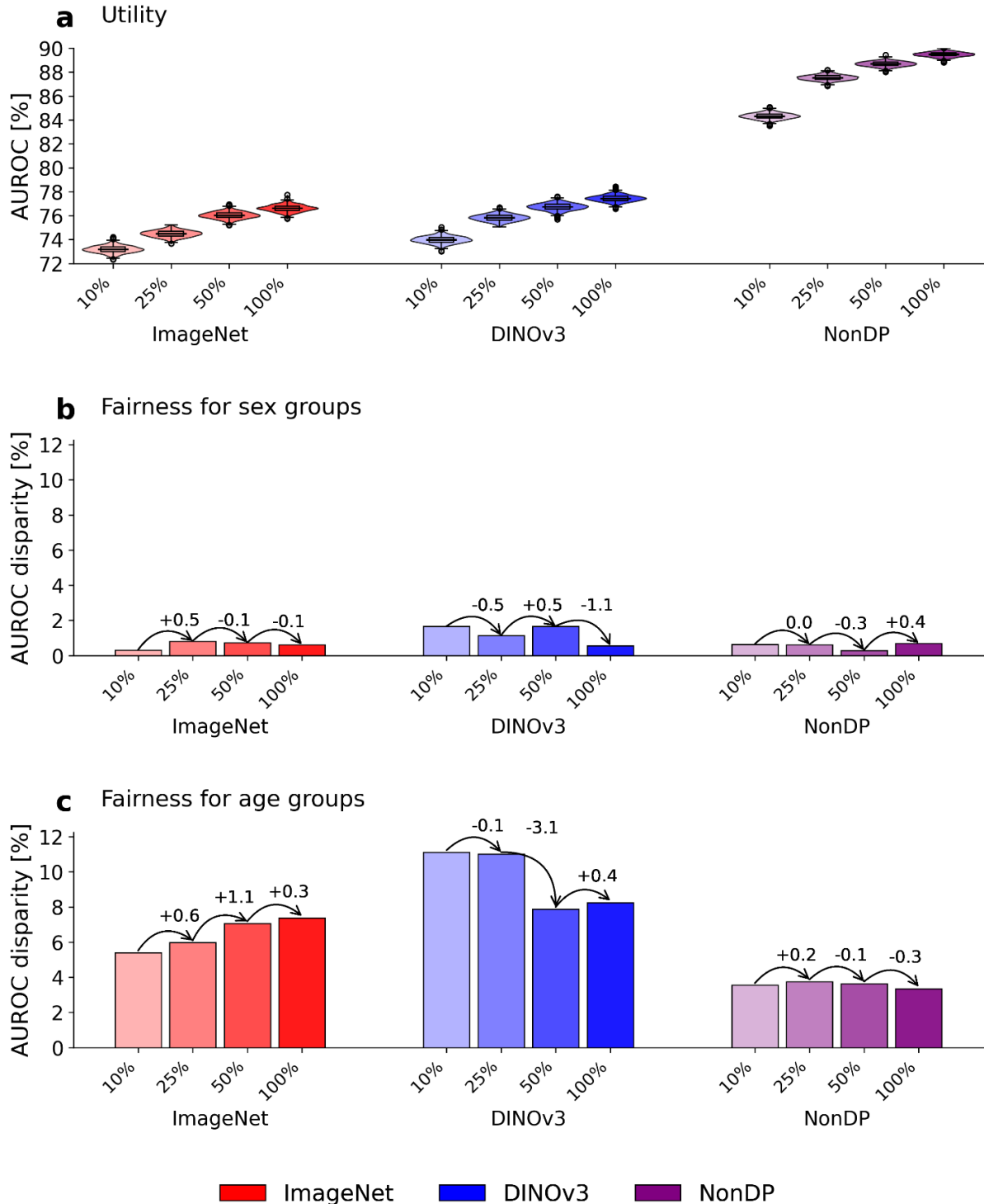


Figure 6: Joint effects of training set size on diagnostic utility and demographic fairness under differential privacy on PadChest. ConvNeXt-Small models are trained on increasing fractions of the PadChest training set (10%: $n = 8,821$; 25%: $n = 22,160$; 50%: $n = 44,072$; 100%: $n = 88,480$) and evaluated on a fixed held-out test set ($n = 22,045$). All differentially private results correspond to the largest privacy range ($3 < \epsilon < 10$), and are compared against a non-private baseline. **a** Violin plots show the distribution of label-averaged AUROC values across 1,000 bootstrap resamples for ImageNet initialization, self-supervised DINOv3 initialization, and non-private training as a function of training set size. **b** Sex-based fairness, quantified as AUROC disparity between male and female subgroups, is shown for the same settings. **c** Age-based fairness, quantified as AUROC disparity across age groups (<40, 40–70, and >70 years), is shown analogously.

As training set size increased, the absolute performance gap between initialization strategies narrowed but did not disappear. At full training set size and larger privacy budgets ($3 < \epsilon < 10$), DINOv3 reached an AUROC of 77.4 ± 0.3 [76.9, 77.9], compared with 76.6 ± 0.3 [76.1, 77.2] for ImageNet initialization ($P < 0.001$). Despite this convergence, both remained well below ($P < 0.001$) the non-private baseline of 89.5 ± 0.2 [89.1, 89.9], demonstrating that increasing dataset size alone does not eliminate the utility cost imposed by DP. Notably, the effect of initialization was largest in the most practically challenging regime, namely small datasets combined with strong privacy guarantees. In these settings, self-supervised initialization yielded improvements comparable in magnitude to those obtained by doubling or tripling the amount of training data under ImageNet initialization ($P < 0.001$). This highlights that initialization and dataset scale act as complementary factors under DP, rather than interchangeable ones.

In addition to diagnostic utility, we evaluated how training set size influences demographic fairness under DP on PadChest using PtD across sex and age groups (**Supplementary Table 4**). Across initialization strategies and privacy regimes, fairness metrics exhibited greater variability at smaller training set sizes, particularly under DP. For sex-based groups, PtD values generally remained within a few percentage points across training sizes. For example, under strong privacy ($0 < \epsilon < 1$) and DINOv3 initialization, male-female PtD decreased in magnitude from 2.1 at 10% of the training data to 1.1 at full dataset size, while ImageNet initialization showed larger disparities over the same range (3.7 at 10% vs. 3.8 at full dataset size). Age-based disparities were larger and more variable than sex-based disparities across all settings, consistent with earlier analyses. Under DP, smaller training sets were associated with pronounced fluctuations in PtD for the oldest age group (>70 years). For instance, under ImageNet initialization at $0 < \epsilon < 1$, PtD for patients over 70 years ranged from -9.7 at 10% of the data to -11.0 at full dataset size, while DINOv3 initialization yielded smaller but still variable values (ranging from -3.6 to -9.0 across training sizes). Increasing training set size generally reduced variability in age-based PtD for DINOv3, although non-negligible disparities persisted even at full dataset size and were also present in the non-private baseline.

3. Discussion

This study provides a large-scale and systematic analysis of how model initialization and pretraining shape the utility, fairness, and robustness of differentially private medical image analysis. Using chest radiograph classification as a representative and well-studied clinical benchmark, we evaluated more than 800,000 images across five datasets, multiple privacy regimes, and complementary experimental settings. Our results clarify a central but previously underexplored conclusion: under DP, initialization is not a secondary implementation detail, but a primary determinant of what levels of performance, fairness, and generalization are achievable.

A key finding is that DP imposes a consistent but strongly initialization-dependent utility cost. While all differentially private models exhibited reduced performance relative to non-private baselines, the magnitude of this degradation varied dramatically across initialization strategies.

Generic supervised ImageNet pretraining proved insufficient to stabilize optimization under DP-SGD, resulting in large and persistent performance gaps across datasets and privacy budgets. In contrast, self-supervised DINOv3 initialization substantially narrowed this gap, demonstrating that modern self-supervised representations learned from natural images can meaningfully support fully private optimization of convolutional networks. However, even at large scale, self-supervised initialization did not recover non-private performance and remained consistently inferior to domain-specific supervised pretraining on large chest radiograph cohorts. Importantly, this hierarchy was preserved across datasets, privacy levels, model capacities, and training set sizes, indicating a stable and interpretable structure to the relationship between initialization and privacy-induced utility loss.

These findings refine the role of SSL in privacy-preserving medical imaging. Prior work has shown that self-supervised representations can rival or surpass ImageNet initialization in non-private settings^{14–17,33}, motivating the expectation that they might similarly close the performance gap introduced by DP. Our results show that this expectation is only partially met. Self-supervised initialization substantially improves feasibility and robustness under DP relative to ImageNet, but does not eliminate the advantage conferred by task-aligned supervised pretraining. This suggests that self-supervised representations capture general visual structure that stabilizes noisy optimization^{12,13}, yet still lack clinically specific features that become critical when gradients are clipped and perturbed throughout training. From a practical perspective, self-supervised pretraining represents a powerful intermediate option when large labeled medical datasets are unavailable, but should not be viewed as a full substitute for domain-specific supervision when such data exist.

Beyond average diagnostic utility, our analysis shows that initialization strongly modulates demographic fairness under DP^{1,2,4,9}. Sex-based disparities remained small across all settings and were largely preserved under privacy constraints, consistent with prior observations in chest radiograph classification. Age-based disparities, by contrast, were substantially larger and exhibited strong dataset dependence, reflecting imbalances already present in non-private models⁸. DP did not introduce age-related disparities where none existed, but amplified them when initialization was poorly aligned with the task. Domain-specific supervised pretraining consistently constrained these effects, while self-supervised initialization reduced but did not fully stabilize threshold-dependent disparities such as equal opportunity and overdiagnosis. These results underscore that fairness outcomes under DP are shaped at least as much by representation quality as by privacy noise itself, and that strong initialization can mitigate the amplification of pre-existing dataset biases.

Our cross-dataset generalization experiments further extend this conclusion. Even when trained on a very large, pooled cohort spanning all evaluation domains, differentially private models exhibited substantial generalization gaps relative to non-private training. Initialization again emerged as the dominant factor governing robustness to distribution shift under privacy constraints. Self-supervised DINOv3 initialization consistently reduced cross-dataset performance loss relative to ImageNet, indicating improved resilience to heterogeneity and privacy noise. However, domain-specific supervised pretraining remained the most effective strategy, limiting generalization degradation across all privacy levels. These findings demonstrate

that data aggregation alone does not overcome privacy-induced optimization challenges, and that initialization plays a critical role in determining whether large-scale training translates into robust deployment under DP.

The stability of these effects across model capacity and training set size reinforces their generality. Reducing model size from 49 million to 28 million parameters resulted in modest absolute performance changes, whereas changing initialization produced substantially larger differences under DP. Similarly, increasing training set size consistently improved diagnostic utility, but did not override the influence of initialization, particularly in low-data and strong-privacy regimes. Notably, self-supervised initialization yielded gains comparable to large increases in training data when ImageNet initialization was used, highlighting that representation quality and data scale act as complementary rather than interchangeable factors in private training. With respect to demographic fairness, increasing training set size reduced variability for some subgroups, particularly for sex-based disparities, but did not fully stabilize fairness outcomes under DP. Age-based disparities remained larger and more variable across training set sizes and privacy regimes, mirroring patterns observed in both the non-private baseline and the main fairness analyses. While self-supervised initialization generally exhibited smaller fluctuations than ImageNet initialization as data scale increased, non-negligible age-related disparities persisted even at full dataset size. These results indicate that, although additional data can improve utility and reduce instability under DP, it does not eliminate fairness disparities that reflect underlying dataset structure and task difficulty.

Several limitations of this study should be acknowledged. First, although our evaluation spans multiple large, predominantly adult chest radiograph datasets, it is limited to image-only classification of a fixed set of thoracic findings. Initialization effects under DP may differ for other clinical tasks, such as localization, segmentation, rare-label prediction, or multimodal settings that integrate imaging with non-imaging data, which should be explored in future work. Second, while we examined supervised and self-supervised pretraining independently, we did not explore hybrid or multi-stage strategies that combine self-supervision with domain-specific supervision, which may further reduce the remaining utility gap under DP. Third, our analysis focused exclusively on convolutional neural networks, motivated by extensive prior evidence that very deep and attention-based architectures remain difficult to train reliably under full-model DP-SGD^{1,2,4,8–10,34}. Previous studies have shown that transformer-based models suffer from severe optimization instability and substantially larger utility degradation under DP, particularly at realistic privacy budgets⁹. Our findings therefore reflect the current practical state of DP training rather than an architectural preference. Importantly, even with task-aligned supervised pretraining, differentially private models remained significantly below non-private performance, in line with prior work^{1,4}. Future methodological advances that improve DP optimization for deeper or more expressive architectures could further improve achievable utility beyond what is currently possible. Fourth, the self-supervised initialization evaluated in this study was derived from pretraining on large-scale non-medical image corpora. While DINOv3 representations demonstrate strong transferability^{26,35,36}, they are learned from data distributions that differ substantially from medical imaging. Self-supervised pretraining on large-scale medical image collections may yield representations that are better aligned with clinical tasks and more robust under DP³³. However,

assembling unlabeled medical datasets at a scale comparable to modern general-domain SSL, which typically involves hundreds of millions of images, remains challenging due to regulatory and institutional constraints. Exploring privacy-aware mechanisms for large-scale medical SSL is therefore an important open problem. Fifth, our fairness analysis was conducted exclusively on held-out test sets, consistent with most prior work in differentially private medical imaging^{1,2,4,8,9}. While this approach captures disparities in deployed model behavior, it does not disentangle how biases emerge during training or how DP alters subgroup-specific learning dynamics. Moreover, our analysis was limited to sex and age groups, which represent only a subset of clinically relevant fairness dimensions. Future work should incorporate more granular subgroup definitions, additional demographic and non-demographic attributes, and training-time analyses to better understand how privacy mechanisms interact with bias formation and mitigation. In addition, some reported metrics, such as accuracy and accuracy-based statistical parity difference, are sensitive to label prevalence, which varies across datasets and demographic subgroups; however, all primary conclusions were supported by prevalence-independent metrics. Finally, our use of domain-specific supervised pretraining assumes the availability of a large, publicly accessible chest radiograph dataset for which privacy concerns are already addressed. While this assumption is standard in prior differentially private medical imaging studies and realistic for chest radiography, it may not hold in other clinical domains where large public datasets are unavailable or privacy constraints preclude such pretraining. In such settings, the relative benefit of domain-specific initialization may be reduced, increasing the practical relevance of self-supervised initialization strategies.

Furthermore, all experiments were conducted at a fixed input resolution of 224×224 pixels. This choice prioritizes training stability and feasibility under full-model DP-SGD, where increasing resolution substantially raises memory and computational demands, amplifies per-sample gradient norms (thereby increasing the impact of clipping), and makes optimization more prone to instability or divergence⁹. Consequently, 224×224 remains a commonly adopted resolution in large-scale differentially private medical imaging studies, including our own prior external validation work⁴. Prior non-private studies in chest radiograph classification have shown that increasing resolution up to 512×512 can yield performance improvements, while gains beyond this point are limited or absent^{16,17,37,38}. Although modest benefits from higher resolution have also been reported in some DP settings, the extent to which such improvements transfer to full-model DP-SGD at the scale and privacy regimes studied here remains uncertain and is likely small relative to the remaining DP-induced utility gap. Addressing resolution scaling under DP therefore represents a broader open challenge that will likely require advances in optimization techniques, memory-efficient training, and DP-compatible architecture design, and is beyond the scope of the present study.

In conclusion, this study demonstrates that initialization choice is a central determinant of diagnostic utility, fairness, and generalization in differentially private medical image analysis. Self-supervised DINOv3 initialization substantially improves robustness and feasibility relative to ImageNet pretraining, particularly in data-limited and high-privacy regimes, but does not fully replace the benefits of large-scale, domain-specific supervised pretraining. These findings provide concrete guidance for practitioners deploying differentially private models in clinical

settings and emphasize that progress in privacy-preserving medical AI depends not only on privacy mechanisms themselves, but on careful alignment between representation learning and the clinical domain.

4. Materials and methods

4.1. Ethics statement

All procedures were conducted in compliance with applicable guidelines and regulations. Ethical approval for this retrospective study was granted by the Ethics Committee of the Medical Faculty of RWTH Aachen University (Reference No. EK 22-319). The committee waived the requirement for individual informed consent.

4.2. Data

This study uses a total of six large-scale chest radiograph datasets, comprising five cohorts used for differentially private training and evaluation and one cohort used exclusively for supervised domain-specific pretraining. In total, the study leverages $n = 805,603$ anteroposterior or posteroanterior chest radiographs, collected across institutions in Asia, Europe, and North America. The datasets reflect diverse clinical environments, including inpatient wards, outpatient care, and intensive care units, and incorporate heterogeneous labeling strategies ranging from expert radiologist annotation to rule-based natural language processing and hybrid approaches.

The five evaluation datasets include VinDr-CXR²⁷, ChestX-ray14²⁸, PadChest²⁹, CheXpert²⁵, and UKA-CXR^{1,4,16,17,30-32}. VinDr-CXR contains $n=18,000$ radiographs acquired at two tertiary hospitals in Vietnam and annotated through independent review by multiple board-certified radiologists. ChestX-ray14 is a large public dataset released by the National Institutes of Health, comprising $n=112,120$ radiographs from over 30,000 patients with labels derived from automated analysis of associated reports. PadChest includes $n=110,525$ radiographs collected at a Spanish academic hospital, with annotations generated through a combination of expert manual labeling and natural language processing. CheXpert consists of $n=157,676$ radiographs acquired at a U.S. academic medical center, with observations extracted using a rule-based report labeling system that distinguishes positive, negative, and uncertain findings. UKA-CXR is an internal dataset from University Hospital RWTH Aachen, comprising $n=193,361$ adult chest radiographs collected primarily in intensive care settings and labeled as part of routine clinical reporting using a structured template. For all evaluation datasets, strictly patient-wise splits were used to separate

training and test cohorts, and these splits were fixed across all initialization strategies and privacy regimes to prevent information leakage.

In addition to the evaluation cohorts, we used the MIMIC-CXR²⁴ dataset as a domain-specific supervised pretraining dataset. MIMIC-CXR contains n=213,921 chest radiographs collected at Beth Israel Deaconess Medical Center in Boston, USA, with labels generated using the same rule-based natural language processing system as CheXpert. ConvNeXt²² models were pretrained on MIMIC-CXR in a supervised manner prior to fine-tuning under DP on the five evaluation datasets. No MIMIC-CXR images were used for model evaluation in this study.

To enable controlled comparison across datasets under DP, all cohorts were harmonized into a unified multilabel classification framework consisting of five labels: atelectasis, cardiomegaly, pleural effusion, pneumonia, and no finding. Only labels present across all datasets were retained. Dataset-specific annotations were binarized following established conventions for each source, with uncertain or ambiguous labels treated as negative where applicable. All images were frontal chest radiographs acquired in anteroposterior or posteroanterior projection. Images were supplied in a mixture of standard image formats and DICOM. For DICOM images, metadata were inspected to ensure correct intensity polarity and corrected when necessary. All radiographs were resized to 224 × 224 pixels, intensity-normalized on a per-image basis, converted to 8-bit grayscale²⁴, and contrast-standardized using histogram equalization to reduce inter-dataset variability arising from differences in acquisition and post-processing^{24,31}.

4.3. Model training

All experiments were conducted using ConvNeXt-based²² convolutional neural networks for multilabel chest radiograph classification. The primary architecture was ConvNeXt-Small, comprising 49,458,533 trainable parameters, which was used for all main experiments. A smaller ConvNeXt-Tiny variant with 27,823,973 parameters was additionally evaluated in a dedicated generalization experiment to assess robustness across model capacity. Both architectures employed a single linear classification head with sigmoid activation to predict multiple thoracic findings simultaneously.

All models were optimized using the AdamW³⁹ optimizer with a weight decay of 0.01. For non-private training, a fixed learning rate of 10^{-5} was used across all datasets and architectures. Training employed standard minibatch stochastic gradient descent, with data augmentation consisting of random horizontal flips and small random rotations. Binary cross-entropy loss was used for multilabel classification, with class weights set inversely proportional to label prevalence in the training data to address class imbalance⁴⁰.

DP training was performed using differentially private stochastic gradient descent (DP-SGD)¹⁰. In this setting, no data augmentation was applied. Models were optimized with AdamW

using learning rates between 5×10^{-6} and 10^{-5} , selected based on convergence behavior under privacy constraints, while maintaining the same weight decay of 0.01 as in non-private training. Instead of conventional minibatching, each data point was independently sampled into a training batch with probability equal to the nominal batch size of 128 divided by the total number of training samples in the dataset, as required for privacy accounting. During DP optimization, per-sample gradients were clipped to a fixed maximum ℓ_2 norm to bound individual contributions. The clipping norm was set to 4 for ConvNeXt-Small and 3.5 for ConvNeXt-Tiny. Gaussian noise was added to the aggregated gradients at each optimization step. A privacy accountant based on Rényi DP⁴¹ was used to track the accumulated privacy loss throughout training. The privacy parameter δ was fixed to 6×10^{-6} for all models, chosen to be smaller than the inverse of the training set size of the largest dataset. The achieved value of ϵ depended on the noise multiplier, the number of optimization steps until convergence, and the effective sampling probability. Reported ϵ values correspond to the privacy budget at the convergence step of each model, reflecting dataset-specific training dynamics^{4,8}.

4.4. Experimental setup

All experiments were conducted within a tightly controlled and standardized framework to enable direct comparison of DP effects across datasets, initialization strategies, and model capacities. For each dataset, patient-wise splits were fixed prior to training and held constant across all experiments, ensuring that no individual contributed images to both training and test sets. Test cohorts were never reused across training configurations, and all reported comparisons were performed on identical held-out samples. This design allowed observed performance differences to be attributed specifically to privacy constraints, initialization choice, dataset scale, or model capacity rather than to variation in data partitioning or evaluation protocol.

To ensure comparability across heterogeneous cohorts, all datasets were mapped to a shared multilabel prediction task consisting of five diagnostic categories: atelectasis, cardiomegaly, pleural effusion, pneumonia, and no finding. Each model was trained to jointly predict the presence or absence of all five findings for a given radiograph. Although the original datasets differ substantially in labeling strategy, prevalence, and clinical context, this harmonized label space enabled consistent evaluation of diagnostic utility under DP across institutions and acquisition settings.

Three distinct initialization regimes were evaluated throughout the study. The first used supervised ImageNet¹⁸ pretraining, representing the conventional baseline in computer vision where models are initialized from labeled natural images. The second used self-supervised DINOv3²⁶ pretraining, in which representations are learned from large-scale natural image collections without access to labels. This initialization was included to test whether modern self-supervised representations can improve the stability and utility of DP training relative to supervised natural image pretraining. The third initialization strategy used supervised domain-specific pretraining on the MIMIC-CXR dataset. For this setting, ConvNeXt models were pretrained on the MIMIC-CXR training set, which contains n=170,153 training chest radiographs

labeled for thoracic findings closely aligned with the downstream tasks. These pretrained weights were then used to initialize models trained under DP on the target datasets. Importantly, all initialization strategies served only as starting points, and all model parameters were subsequently fine-tuned during downstream training.

DP was evaluated across three predefined privacy ranges, in addition to a non-private ($\epsilon = \infty$) baseline. Privacy budgets were grouped into $0 < \epsilon < 1$, $1 < \epsilon < 3$, and $3 < \epsilon < 10$. These ranges were selected to reflect commonly studied operating regimes in the medical privacy literature and to capture a spectrum from very stringent privacy constraints to more permissive yet still formally private settings. Reporting results by privacy range, rather than by a single fixed ϵ , accounts for differences in dataset size, training duration, and convergence behavior, while allowing meaningful comparison of trends across datasets and models.

All experiments were performed using identical optimization objectives, evaluation metrics, and stopping criteria within each privacy regime. Primary analyses focused on ConvNeXt-Small as reference architecture, with additional experiments using ConvNeXt-Tiny to assess the robustness of observed trends across model capacity. Across all settings, performance was evaluated on held-out test sets using AUROC as the primary metric, averaged across the five labels, with additional metrics reported for completeness.

4.5. Experiments

A series of complementary experiments was conducted to characterize how DP interacts with model initialization, dataset heterogeneity, model capacity, and training set size in chest radiograph classification. All experiments used the standardized datasets, label space, preprocessing pipeline, and training procedures described above, with patient-wise splits fixed across configurations to ensure comparability.

The primary set of experiments focused on diagnostic utility under DP across individual datasets. For each of the five datasets, ConvNeXt-Small models were trained independently under non-private conditions and under three predefined privacy ranges. Each training run was repeated for all three initialization strategies, resulting in a comprehensive comparison of privacy-utility trade-offs across datasets that vary widely in size, label prevalence, and acquisition context. This experiment was designed to assess whether the effects of DP are consistent across institutions and to quantify how initialization influences optimization stability and attainable performance under privacy constraints.

To examine demographic fairness, subgroup analyses were performed for sex and age on the held-out test sets of each dataset. Models trained under the same configurations as in the primary utility experiments were evaluated separately for each demographic subgroup. Fairness analyses were conducted across all initialization strategies and privacy ranges, enabling

assessment of whether DP systematically alters subgroup performance or amplifies existing dataset imbalances. These experiments were designed to isolate demographic effects without modifying training procedures or introducing additional fairness-specific optimization.

Robustness to distribution shift was evaluated using a cross-dataset generalization experiment. In this setting, a single ConvNeXt-Small model was trained on the combined training cohorts of all five datasets, forming a large and heterogeneous training set ($n = 471,896$). The resulting model was then evaluated independently on the test set of each dataset, including VinDr-CXR (test $n = 3,000$), ChestX-ray14 (test $n = 25,596$), PadChest (test $n = 22,045$), CheXpert (test $n = 29,321$), and UKA-CXR (test $n = 39,824$). This experiment was repeated across initialization strategies and privacy ranges, and compared against a non-private baseline. The goal of this experiment was to assess whether initialization strategies that stabilize private training in-domain also improve generalization across institutional and distributional boundaries under DP.

To determine whether observed effects depend on model capacity, an additional set of experiments compared ConvNeXt-Small with the smaller ConvNeXt-Tiny architecture. Both architectures were evaluated under identical conditions, including the same datasets, initialization strategies, and privacy ranges. This experiment tested whether privacy-induced degradation and initialization effects scale consistently with model size, or whether they are specific to a particular architectural capacity.

Finally, the interaction between training set size and DP was investigated using PadChest as a representative large-scale dataset. ConvNeXt-Small models were trained on progressively larger fractions of the PadChest training set (10%: $n = 8,821$, 25%: $n = 22,160$, 50%: $n = 44,072$, 100%: $n = 88,480$) while keeping the test set fixed ($n = 22,045$). This experiment was conducted across initialization strategies and privacy ranges, enabling assessment of how data availability modulates the impact of privacy noise and whether strong initialization can compensate for limited training data. This setting reflects practical scenarios in medical imaging where dataset size is constrained and privacy requirements are stringent.

4.6. Evaluation

Model performance was evaluated using a combination of threshold-independent and threshold-dependent utility metrics. The primary metric was the area under the receiver operating characteristic curve (AUROC), which provides a threshold-independent measure of discrimination in multilabel classification. For each dataset and experimental configuration, AUROC was computed separately for each of the five labels, including atelectasis, cardiomegaly, pleural effusion, pneumonia, and no finding, and then averaged to obtain a single summary AUROC per model. Label-averaged AUROC values are reported in the main manuscript for conciseness, while full per-label AUROC results are provided in the supplementary information. Accuracy, sensitivity, and specificity were reported as secondary utility metrics to characterize clinically

relevant operating points. Classification thresholds were selected using Youden's index⁴², defined as the threshold that maximizes the difference between the true positive rate and false positive rate on the test set.

To assess demographic fairness under DP, multiple complementary disparity metrics were computed across demographic subgroups⁹. Fairness analyses were performed independently for each dataset, initialization strategy, and privacy regime using subgroup-specific performance estimates derived from the same held-out test sets. Differences in discriminatory performance between demographic groups were quantified using AUROC disparity. For a set of demographic subgroups $\{g_1, g_2, \dots, g_k\}$, AUROC disparity was defined as:

$$\Delta\text{AUROC} = \max_{i \neq j} |\text{AUROC}_{g_i} - \text{AUROC}_{g_j}|. \quad (1)$$

Subgroup-specific AUROC values were computed by averaging AUROC across diagnostic labels prior to disparity calculation.

Differences in sensitivity, reflecting disparities in true positive rates across demographic groups, were quantified using equal opportunity difference (EOD)⁴³, defined as

$$\text{EOD} = \max_{i \neq j} |\text{Sens}_{g_i} - \text{Sens}_{g_j}|, \quad (2)$$

where Sens_{g_i} denotes the label-averaged sensitivity for subgroup g_i .

To capture differences in false positive behavior between demographic groups, overdiagnosis disparity (OD) was computed based on false positive rates (FPRs). The FPR was defined as:

$$\text{FPR} = 1 - \text{Specificity}. \quad (3)$$

OD was then defined as:

$$\text{OD} = \max_{i \neq j} |\text{FPR}_{g_i} - \text{FPR}_{g_j}| = \max_{i \neq j} |\text{Spec}_{g_i} - \text{Spec}_{g_j}|. \quad (4)$$

Specificity values were averaged across diagnostic labels within each subgroup before computing disparities.

In addition to absolute disparity measures, statistical parity difference (PtD) was computed on accuracy to capture signed performance differences between demographic groups^{8,44,45}. For binary demographic attributes, PtD was defined symmetrically as:

$$\text{PtD}(g_1) = \text{Acc}_{g_1} - \text{Acc}_{g_2}, \quad \text{PtD}(g_2) = \text{Acc}_{g_2} - \text{Acc}_{g_1}. \quad (5)$$

For demographic attributes with more than two groups, PtD was computed using a one-vs-rest formulation to account for unequal subgroup sizes. Let subgroup g_i have accuracy A_i and sample size n_i . PtD for subgroup g_i was defined as:

$$\text{PtD}(g_i) = A_i - \frac{\sum_{j \neq i} n_j A_j}{\sum_{j \neq i} n_j}. \quad (6)$$

Because accuracy depends on label prevalence, which varies across datasets and demographic subgroups, accuracy-based results were interpreted with caution. Primary conclusions regarding diagnostic performance and fairness were therefore drawn from prevalence-independent metrics (AUROC, sensitivity, and specificity), with accuracy and accuracy-based fairness measures (PtD) included to reflect clinically intuitive behavior under realistic class imbalance.

4.7. Statistical analysis

All statistical analyses were performed in Python 3.10 using NumPy 2.2, SciPy 1.15, and scikit-learn 1.7, pandas 2.3. Model utility and fairness metrics were estimated using nonparametric bootstrapping with 1,000 resamples of the held-out test sets. Resampling was performed at the patient level to preserve correlations among multiple images from the same individual. For each experimental configuration, we report the mean and standard deviation of the bootstrap distribution together with 95% confidence intervals computed using the percentile method^{16,46}. Comparisons between initialization strategies, privacy regimes, and model variants were conducted using paired bootstrap resampling. Strictly identical bootstrap samples were applied across models evaluated on the same dataset, ensuring that observed performance differences reflect model behavior rather than sampling variability. Statistical significance of differences in diagnostic performance was assessed using paired bootstrap tests on label-averaged AUROC values^{16,17,30,47}. To control for multiple hypothesis testing across datasets, privacy regimes, and initialization strategies, p-values were adjusted within coherent families of related comparisons using the Benjamini-Hochberg false discovery rate (FDR) procedure. An FDR-adjusted p-value below 0.05 was considered statistically significant⁴⁸. This statistical analysis framework was applied consistently across all reported utility and fairness results to support reliable inference under the large number of experimental conditions examined in this study. For p-values ≥ 0.001 , values are reported with two significant figures; smaller p-values are reported as $P < 0.001$.

4.8. Data, code, and model availability

This study draws on a combination of publicly available datasets, controlled-access resources, and an institutional clinical cohort. ChestX-ray14 and PadChest are openly accessible datasets and can be obtained from their respective public repositories at <https://www.kaggle.com/datasets/nih-chest-xrays/data> and <https://bimcv.cipf.es/bimcv-projects/padchest/>. VinDr-CXR and MIMIC-CXR are distributed under controlled access via PhysioNet and require completion of the corresponding data use agreements prior to download

at <https://physionet.org/content/vindr-cxr/1.0.0/> and <https://physionet.org/content/mimic-cxr-jpg/2.0.0/>. The CheXpert dataset is available upon request from Stanford University through <https://stanfordmlgroup.github.io/competitions/chexpert/>. The UKA-CXR dataset comprises clinical imaging data collected at University Hospital RWTH Aachen, Germany. Access to the full cohort is subject to institutional approval and may be granted upon reasonable request to the corresponding authors under a formal collaboration agreement. In addition, a subset of the UKA-CXR dataset has been released publicly and is available through the Hugging Face platform at <https://huggingface.co/TLAIM>.

All source code, configuration files, and instructions required to reproduce the experiments are publicly available at https://github.com/tayebiarasteh/dp_dinov3. Training and evaluation were performed strictly in full 32-bit floating point precision. Experiments were conducted between October 27, 2025, and December 17, 2025. The implementation was based on Python 3.10 using PyTorch 2.5 and torchvision 0.20. Core scientific computing libraries included NumPy 2.2, SciPy 1.15, scikit-learn 1.7, pandas 2.3, Opacus 1.5, and OpenCV 4.12. Hugging Face tooling comprised transformers 4.56, huggingface-hub 0.34, accelerate 1.10, tokenizers 0.21, and safetensors 0.6.

All pretrained initialization weights were obtained from official public repositories hosted on Hugging Face. Supervised ImageNet initialization used ConvNeXt-Tiny and ConvNeXt-Small models available at <https://huggingface.co/facebook/convnext-tiny-224> and <https://huggingface.co/facebook/convnext-small-224>. Self-supervised initialization used DINOv3-pretrained ConvNeXt models released by Meta AI, specifically <https://huggingface.co/facebook/dinov3-convnext-small-pretrain-lvd1689m> and <https://huggingface.co/facebook/dinov3-convnext-tiny-pretrain-lvd1689m>. All pretrained weights were loaded directly from these repositories without modification.

5. Acknowledgements

S.N. was supported by grants from the Deutsche Forschungsgemeinschaft (DFG) (NE 2136/3-1, LI3893/6- 1, TR 1700/7-1). D.T. was supported by grants from the DFG (NE 2136/3-1, LI3893/6-1, TR 1700/7-1) and is supported by the German Federal Ministry of Education (TRANSFORM LIVER, 031L0312A; SWAG, 01KD2215B) and the European Union’s Horizon Europe and innovation programme (ODELIA [Open Consortium for Decentralized Medical Artificial Intelligence], 101057091).

6. Author contributions

The formal analysis and conceptualization were conducted by S.T.A. and D.T.. The original draft was written by S.T.A., M.F., and M.L.. The code was developed by S.T.A.. The experiments were

performed by S.T.A.. The illustrations were designed by M.F.. The statistical analyses were performed by S.T.A., M.F., S.N., and D.T.. B.H.P., C.K., S.N., and D.T. provided clinical expertise. The study was defined by S.T.A.. All authors read the manuscript, agreed to the submission of this paper, and contributed to the editing.

7. Competing interests

S.T.A. is an editorial board at *Communications Medicine* and at *European Radiology Experimental*, and a trainee editorial board at *Radiology: Artificial Intelligence*. B.H.P. is an associate editor at *Journal of Medical Internet Research*. D.T. received honoraria for lectures by Bayer, GE, Roche, AstraZeneca, and Philips and holds shares in StratifAI GmbH, Germany, and in Synagen GmbH, Germany. The other authors do not have any competing interests to disclose.

References

1. Tayebi Arasteh, S. *et al.* Preserving fairness and diagnostic accuracy in private large-scale AI models for medical imaging. *Commun Med* **4**, 46 (2024).
2. Kaassis, G. *et al.* End-to-end privacy preserving deep learning on multi-institutional medical imaging. *Nat Mach Intell* **3**, 473–484 (2021).
3. Balle, B., Cherubin, G. & Hayes, J. Reconstructing Training Data with Informed Adversaries. in *2022 IEEE Symposium on Security and Privacy (SP)* 1138–1156 (IEEE, San Francisco, CA, USA, 2022). doi:10.1109/SP46214.2022.9833677.
4. Tayebi Arasteh, S. *et al.* Securing Collaborative Medical AI by Using Differential Privacy: Domain Transfer for Classification of Chest Radiographs. *Radiology. Artificial Intelligence* **6**, e230212 (2024).
5. Dwork, C. Differential Privacy. in *Automata, Languages and Programming* (eds Bugliesi, M., Preneel, B., Sassone, V. & Wegener, I.) vol. 4052 1–12 (Springer Berlin Heidelberg, Berlin, Heidelberg, 2006).
6. De, S., Berrada, L., Hayes, J., Smith, S. L. & Balle, B. Unlocking High-Accuracy Differentially Private Image Classification through Scale. Preprint at <http://arxiv.org/abs/2204.13650> (2022).
7. Kurakin, A. *et al.* Toward Training at ImageNet Scale with Differential Privacy. Preprint at <http://arxiv.org/abs/2201.12328> (2022).
8. Tayebi Arasteh, S. *et al.* Differential privacy enables fair and accurate AI-based analysis of speech disorders while protecting patient data. *npj Artificial Intelligence* **1**, 37 (2025).
9. Mohammadi, M. *et al.* Differential privacy for medical deep learning: methods, tradeoffs, and deployment implications. *npj Digit. Med.* **9**, (2026).
10. Abadi, M. *et al.* Deep Learning with Differential Privacy. in *Proceedings of the 2016 ACM SIGSAC Conference on Computer and Communications Security* 308–318 (ACM, Vienna Austria, 2016). doi:10.1145/2976749.2978318.
11. Ziller, A. *et al.* Reconciling privacy and accuracy in AI for medical imaging. *Nat Mach Intell* **6**, 764–774 (2024).

12. Krishnan, R., Rajpurkar, P. & Topol, E. J. Self-supervised learning in medicine and healthcare. *Nat. Biomed. Eng* **6**, 1346–1352 (2022).
13. Hendrycks, D., Mazeika, M., Kadavath, S. & Song, D. Using self-supervised learning can improve model robustness and uncertainty. in *NIPS'19: Proceedings of the 33rd International Conference on Neural Information Processing Systems* vol. 1403 15663–15674 (2019).
14. Yang, S., Wang, H., Xing, Z., Chen, S. & Zhu, L. SegDINO: An Efficient Design for Medical and Natural Image Segmentation with DINO-V3. Preprint at <https://doi.org/10.48550/arXiv.2509.00833> (2025).
15. Li, Y., Wu, Y., Lai, Y., Hu, M. & Yang, X. MedDINOv3: How to adapt vision foundation models for medical image segmentation? Preprint at <https://doi.org/10.48550/arXiv.2509.02379> (2025).
16. Tayebi Arasteh, S., Misera, L., Kather, J. N., Truhn, D. & Nebelung, S. Enhancing diagnostic deep learning via self-supervised pretraining on large-scale, unlabeled non-medical images. *Eur Radiol Exp* **8**, 10 (2024).
17. Tayebi Arasteh, S. *et al.* Resolution scaling governs DINOv3 transfer performance in chest radiograph classification. Preprint at <https://doi.org/10.48550/arXiv.2510.07191> (2025).
18. Deng, J. *et al.* ImageNet: A large-scale hierarchical image database. in *2009 IEEE Conference on Computer Vision and Pattern Recognition* 248–255 (IEEE, Miami, FL, 2009). doi:10.1109/CVPR.2009.5206848.
19. Ke, A., Ellsworth, W., Banerjee, O., Ng, A. Y. & Rajpurkar, P. CheXtransfer: performance and parameter efficiency of ImageNet models for chest X-Ray interpretation. in *Proceedings of the Conference on Health, Inference, and Learning* 116–124 (ACM, Virtual Event USA, 2021). doi:10.1145/3450439.3451867.
20. Vaswani, A. *et al.* Attention Is All You Need. in *NIPS'17: Proceedings of the 31st International Conference on Neural Information Processing Systems* 6000–6010 (2017).
21. Dosovitskiy, A. *et al.* An Image is Worth 16x16 Words: Transformers for Image Recognition at Scale. Preprint at <http://arxiv.org/abs/2010.11929> (2021).
22. Liu, Z. *et al.* A convnet for the 2020s. in *Proceedings of the IEEE/CVF conference on computer vision and pattern recognition* 11976–11986 (2022).
23. Tayebi Arasteh, S. *et al.* The Treasure Trove Hidden in Plain Sight: The Utility of GPT-4 in Chest Radiograph Evaluation. *Radiology* **313**, e233441 (2024).
24. Johnson, A. E. W. *et al.* MIMIC-CXR, a de-identified publicly available database of chest radiographs with free-text reports. *Sci Data* **6**, 317 (2019).
25. Irvin, J. *et al.* CheXpert: A Large Chest Radiograph Dataset with Uncertainty Labels and Expert Comparison. *AAAI* **33**, 590–597 (2019).
26. Siméoni, O. *et al.* DINOv3. Preprint at <https://doi.org/10.48550/arXiv.2508.10104> (2025).
27. Nguyen, H. Q. *et al.* VinDr-CXR: An open dataset of chest X-rays with radiologist's annotations. *Sci Data* **9**, 429 (2022).
28. Wang, X. *et al.* ChestX-ray8: Hospital-scale Chest X-ray Database and Benchmarks on Weakly-Supervised Classification and Localization of Common Thorax Diseases. in *2017 IEEE Conference on Computer Vision and Pattern Recognition (CVPR)* 3462–3471 (2017). doi:10.1109/CVPR.2017.369.
29. Bustos, A., Pertusa, A., Salinas, J.-M. & de la Iglesia-Vayá, M. PadChest: A large chest x-ray image dataset with multi-label annotated reports. *Medical Image Analysis* **66**, 101797 (2020).
30. Khader, F. *et al.* Artificial Intelligence for Clinical Interpretation of Bedside Chest Radiographs. *Radiology* **307**, e220510 (2022).
31. Tayebi Arasteh, S. *et al.* Collaborative training of medical artificial intelligence models with non-uniform labels. *Sci Rep* **13**, 6046 (2023).

32. Tayebi Arasteh, S., Isfort, P., Kuhl, C., Nebelung, S. & Truhn, D. Automatic Evaluation of Chest Radiographs – The Data Source Matters, But How Much Exactly? in *RöFo-Fortschritte auf dem Gebiet der Röntgenstrahlen und der bildgebenden Verfahren* vol. 195 ab99 (Georg Thieme Verlag, RheinMain CongressCenter (RMCC) in Wiesbaden, 2023).
33. Lotfinia, M., Tayebiarasteh, A., Samiei, S., Joodaki, M. & Tayebi Arasteh, S. Boosting multi-demographic federated learning for chest radiograph analysis using general-purpose self-supervised representations. *European Journal of Radiology Artificial Intelligence* **3**, 100028 (2025).
34. Ziller, A. *et al.* Medical imaging deep learning with differential privacy. *Sci Rep* **11**, 13524 (2021).
35. Caron, M. *et al.* Emerging Properties in Self-Supervised Vision Transformers. in *Proceedings of the IEEE/CVF International Conference on Computer Vision (ICCV)* 9650–9660 (2021).
36. Oquab, M. *et al.* DINOv2: Learning Robust Visual Features without Supervision. Preprint at <http://arxiv.org/abs/2304.07193> (2023).
37. Sabottke, C. F. & Spieler, B. M. The Effect of Image Resolution on Deep Learning in Radiography. *Radiology: Artificial Intelligence* **2**, e190015 (2020).
38. Haque, M. I. U. *et al.* Effect of image resolution on automated classification of chest X-rays. *J Med Imaging (Bellingham)* **10**, 044503 (2023).
39. Loshchilov, I. & Hutter, F. Decoupled Weight Decay Regularization. in *Proceedings of Seventh International Conference on Learning Representations (ICLR) 2019* (New Orleans, LA, USA, 2019).
40. Rezaei-Dastjerdehei, M. R., Mijani, A. & Fatemizadeh, E. Addressing Imbalance in Multi-Label Classification Using Weighted Cross Entropy Loss Function. in *2020 27th National and 5th International Iranian Conference on Biomedical Engineering (ICBME)* 333–338 (IEEE, Tehran, Iran, 2020). doi:10.1109/ICBME51989.2020.9319440.
41. Mironov, I. Rényi Differential Privacy. in *2017 IEEE 30th Computer Security Foundations Symposium (CSF)* 263–275 (IEEE, Santa Barbara, CA, 2017). doi:10.1109/CSF.2017.11.
42. Unal, I. Defining an Optimal Cut-Point Value in ROC Analysis: An Alternative Approach. *Comput Math Methods Med* **2017**, 3762651 (2017).
43. Hardt, M., Price, E. & Srebro, N. Equality of opportunity in supervised learning. *Advances in neural information processing systems* **29**, (2016).
44. Calders, T. & Verwer, S. Three naive Bayes approaches for discrimination-free classification. *Data Min Knowl Disc* **21**, 277–292 (2010).
45. Dwork, C., Hardt, M., Pitassi, T., Reingold, O. & Zemel, R. Fairness through awareness. in *Proceedings of the 3rd Innovations in Theoretical Computer Science Conference* 214–226 (ACM, Cambridge Massachusetts, 2012). doi:10.1145/2090236.2090255.
46. Konietzschke, F. & Pauly, M. Bootstrapping and permuting paired t-test type statistics. *Stat Comput* **24**, 283–296 (2014).
47. Tayebi Arasteh, S. *et al.* Enhancing domain generalization in the AI-based analysis of chest radiographs with federated learning. *Sci Rep* **13**, 22576 (2023).
48. Tayebi Arasteh, S. *et al.* RadioRAG: Online Retrieval–Augmented Generation for Radiology Question Answering. *Radiology: Artificial Intelligence* **7**, e240476 (2025).

Supplementary information

Supplementary Table 1: Utility of differentially private ConvNeXt-Tiny models across datasets, privacy levels, and initialization strategies. Model utility is evaluated using the area under the receiver operating characteristic curve (AUROC), accuracy, specificity, and sensitivity, each computed from 1,000 bootstrap resamples and averaged across five labels, including atelectasis, cardiomegaly, pleural effusion, pneumonia, and no finding. ConvNeXt-Tiny models were trained under three differential privacy (DP) regimes ($0 < \epsilon < 1$, $1 < \epsilon < 3$, and $3 < \epsilon < 10$) and compared against a non-private baseline ($\epsilon = \infty$). Results are reported for three initialization strategies: DINOv3, ImageNet, and domain-specific pretrained weights, based on MIMIC-CXR dataset (n=213,921). Performance is evaluated on five chest radiograph datasets: VinDr-CXR (training n = 15,000; test n = 3,000), ChestX-ray14 (training n = 86,524; test n = 25,596), PadChest (training n = 88,480; test n = 22,045), CheXpert (training n = 128,355; test n = 29,321), and UKA-CXR (training n = 153,537; test n = 39,824). Values are presented in percent as mean \pm standard deviation with corresponding 95% confidence intervals.

Initialization	Metric [%]	Epsilon	VinDr-CXR	ChestX-ray14	PadChest	CheXpert	UKA-CXR
DinoV3	AUROC	$0 < \epsilon < 1$	78.1 ± 1.1 [75.7, 80.1]	64.0 ± 0.3 [63.3, 64.7]	75.2 ± 0.3 [74.6, 75.7]	69.8 ± 0.2 [69.3, 70.3]	78.8 ± 0.2 [78.5, 79.1]
		$1 < \epsilon < 3$	78.3 ± 1.1 [76.2, 80.3]	64.3 ± 0.3 [63.7, 65.0]	75.6 ± 0.3 [75.1, 76.2]	69.7 ± 0.2 [69.2, 70.2]	79.5 ± 0.2 [79.2, 79.8]
		$3 < \epsilon < 10$	80.2 ± 1.0 [78.2, 82.1]	65.6 ± 0.3 [65.0, 66.3]	77.0 ± 0.3 [76.4, 77.5]	71.3 ± 0.3 [70.8, 71.8]	81.8 ± 0.1 [81.5, 82.1]
	Accuracy	$0 < \epsilon < 1$	75.9 ± 1.6 [72.8, 78.8]	49.4 ± 2.5 [45.6, 54.0]	66.8 ± 1.2 [64.0, 69.1]	65.5 ± 4.1 [60.1, 73.8]	71.6 ± 0.5 [70.6, 72.3]
		$1 < \epsilon < 3$	71.2 ± 2.1 [67.8, 75.7]	55.0 ± 2.4 [50.0, 59.5]	69.0 ± 1.6 [65.7, 72.4]	69.5 ± 5.2 [57.6, 76.0]	72.5 ± 0.7 [71.1, 73.7]
		$3 < \epsilon < 10$	0.9 ± 1.9 [67.3, 74.6]	59.1 ± 2.4 [53.9, 62.4]	72.5 ± 1.2 [70.4, 74.9]	69.5 ± 2.7 [64.1, 74.4]	74.9 ± 0.4 [74.2, 75.9]
	Specificity	$0 < \epsilon < 1$	75.7 ± 1.8 [71.9, 78.8]	48.8 ± 3.2 [43.9, 54.6]	66.3 ± 1.4 [63.2, 68.9]	65.2 ± 4.4 [59.0, 74.4]	71.1 ± 0.7 [69.7, 72.3]
		$1 < \epsilon < 3$	70.2 ± 2.3 [66.4, 75.2]	55.7 ± 2.7 [50.2, 60.7]	68.7 ± 1.7 [65.1, 72.4]	69.6 ± 5.6 [56.8, 76.8]	72.3 ± 1.0 [70.4, 74.3]
		$3 < \epsilon < 10$	70.0 ± 2.0 [66.2, 74.1]	59.9 ± 2.6 [54.3, 63.7]	73.0 ± 1.3 [70.6, 75.7]	69.6 ± 3.0 [63.7, 75.2]	75.2 ± 0.6 [74.1, 76.6]
	Sensitivity	$0 < \epsilon < 1$	71.2 ± 2.3 [66.9, 75.6]	73.2 ± 3.1 [67.2, 77.9]	74.2 ± 1.4 [71.5, 77.0]	66.2 ± 4.5 [56.8, 72.4]	72.9 ± 0.7 [71.6, 74.3]
		$1 < \epsilon < 3$	75.6 ± 2.5 [70.3, 79.9]	66.7 ± 2.6 [61.6, 72.0]	72.7 ± 1.8 [68.8, 76.1]	62.0 ± 5.6 [54.6, 74.6]	73.1 ± 1.0 [71.1, 75.0]
		$3 < \epsilon < 10$	78.4 ± 2.4 [73.1, 82.3]	64.2 ± 2.5 [60.3, 69.8]	71.0 ± 1.4 [68.0, 73.4]	64.5 ± 3.0 [58.6, 70.3]	74.2 ± 0.7 [72.7, 75.3]
ImageNet	AUROC	$0 < \epsilon < 1$	69.3 ± 1.2 [67.0, 71.6]	60.4 ± 0.3 [59.8, 61.1]	75.3 ± 0.3 [74.7, 75.8]	67.9 ± 0.3 [67.3, 68.4]	73.2 ± 0.2 [72.8, 73.6]
		$1 < \epsilon < 3$	72.0 ± 1.1 [69.7, 74.2]	60.3 ± 0.3 [59.7, 61.0]	76.4 ± 0.3 [75.8, 76.9]	67.8 ± 0.3 [67.3, 68.3]	76.6 ± 0.2 [76.3, 76.9]
		$3 < \epsilon < 10$	79.6 ± 1.0 [77.6, 81.5]	63.0 ± 0.3 [62.3, 63.7]	76.6 ± 0.3 [76.0, 77.1]	69.8 ± 0.2 [69.3, 70.3]	81.7 ± 0.1 [81.4, 82.0]
	Accuracy	$0 < \epsilon < 1$	69.6 ± 3.2 [62.8, 75.6]	46.3 ± 1.9 [42.8, 50.0]	66.2 ± 0.9 [64.2, 67.8]	62.9 ± 3.2 [57.2, 68.4]	65.7 ± 0.7 [64.2, 66.9]
		$1 < \epsilon < 3$	68.5 ± 3.5 [60.9, 74.0]	45.5 ± 2.1 [40.6, 49.5]	68.0 ± 1.4 [65.5, 71.1]	61.3 ± 2.5 [56.1, 65.4]	69.3 ± 0.4 [68.4, 70.1]
		$3 < \epsilon < 10$	70.3 ± 2.7 [64.9, 75.2]	47.2 ± 1.7 [45.0, 51.1]	68.0 ± 1.2 [65.8, 70.1]	61.5 ± 5.2 [54.1, 70.4]	72.5 ± 0.6 [71.4, 73.6]
	Specificity	$0 < \epsilon < 1$	68.1 ± 3.8 [60.8, 75.2]	44.5 ± 2.2 [40.2, 48.8]	65.2 ± 1.1 [62.9, 67.2]	61.0 ± 3.5 [54.4, 67.1]	64.2 ± 1.0 [62.1, 66.0]
		$1 < \epsilon < 3$	65.8 ± 4.1 [57.2, 73.3]	43.6 ± 2.3 [38.3, 48.0]	67.1 ± 1.5 [64.3, 70.4]	59.0 ± 2.8 [53.0, 63.8]	69.3 ± 0.7 [67.7, 70.7]
		$3 < \epsilon < 10$	70.5 ± 2.9 [64.9, 75.8]	46.3 ± 1.9 [43.5, 50.5]	67.4 ± 1.3 [65.0, 69.7]	60.0 ± 5.6 [51.7, 69.7]	71.4 ± 0.8 [69.8, 73.0]
	Sensitivity	$0 < \epsilon < 1$	63.1 ± 4.0 [55.3, 70.8]	73.3 ± 2.2 [68.9, 77.4]	75.5 ± 1.2 [73.3, 77.8]	67.1 ± 3.6 [60.7, 73.7]	70.4 ± 1.0 [68.7, 72.6]
		$1 < \epsilon < 3$	69.3 ± 4.1 [61.7, 77.0]	73.9 ± 2.2 [69.4, 78.7]	74.9 ± 1.6 [71.5, 77.8]	68.8 ± 2.8 [63.9, 74.6]	71.4 ± 0.8 [69.8, 73.1]
		$3 < \epsilon < 10$	76.3 ± 2.7 [71.1, 81.4]	74.9 ± 1.9 [70.3, 77.6]	76.8 ± 1.4 [74.2, 79.3]	71.0 ± 5.5 [61.3, 79.0]	77.4 ± 0.8 [75.9, 79.0]

Supplementary Table 1: continued.

Initialization	Metric [%]	Epsilon	VinDr-CXR	ChestX-ray14	PadChest	CheXpert	UKA-CXR
Domain-specific	AUROC	$0 < \epsilon < 1$	92.5 ± 0.6 [91.3, 93.6]	74.9 ± 0.3 [74.2, 75.4]	84.6 ± 0.2 [84.1, 85.1]	76.0 ± 0.2 [75.5, 76.5]	84.9 ± 0.1 [84.6, 85.2]
		$1 < \epsilon < 3$	92.3 ± 0.5 [91.2, 93.4]	75.1 ± 0.3 [74.4, 75.7]	85.3 ± 0.2 [84.9, 85.8]	75.6 ± 0.2 [75.1, 76.0]	85.4 ± 0.1 [85.1, 85.6]
		$3 < \epsilon < 10$	92.5 ± 0.6 [91.3, 93.6]	75.4 ± 0.3 [74.8, 76.0]	85.8 ± 0.2 [85.3, 86.2]	76.4 ± 0.2 [75.9, 76.9]	85.5 ± 0.1 [85.2, 85.7]
	Accuracy	$0 < \epsilon < 1$	87.4 ± 0.8 [85.5, 88.8]	67.2 ± 1.9 [64.1, 72.0]	77.6 ± 0.9 [76.0, 79.4]	69.8 ± 1.7 [66.0, 72.4]	75.1 ± 0.3 [74.5, 75.8]
		$1 < \epsilon < 3$	86.3 ± 1.1 [84.1, 88.5]	69.0 ± 1.9 [65.4, 72.3]	78.3 ± 0.8 [76.7, 79.7]	67.9 ± 1.2 [65.9, 70.4]	76.5 ± 0.5 [75.5, 77.7]
		$3 < \epsilon < 10$	86.1 ± 1.0 [84.1, 88.2]	68.2 ± 1.2 [65.8, 70.4]	79.2 ± 0.7 [77.8, 80.4]	69.2 ± 2.2 [66.5, 74.1]	77.1 ± 0.4 [76.3, 78.0]
	Specificity	$0 < \epsilon < 1$	85.9 ± 0.9 [83.8, 87.6]	69.1 ± 2.1 [65.5, 74.5]	77.2 ± 1.0 [75.3, 79.3]	68.9 ± 2.0 [64.5, 72.4]	74.4 ± 0.5 [73.4, 75.6]
		$1 < \epsilon < 3$	85.3 ± 1.2 [83.1, 87.8]	70.7 ± 2.1 [66.7, 74.4]	78.0 ± 0.9 [76.1, 79.6]	66.2 ± 1.5 [63.7, 69.2]	76.6 ± 0.8 [75.0, 78.3]
		$3 < \epsilon < 10$	84.5 ± 1.2 [82.3, 87.0]	69.9 ± 1.5 [66.9, 72.6]	79.1 ± 0.8 [77.4, 80.5]	67.9 ± 2.4 [64.7, 73.6]	77.5 ± 0.6 [76.4, 78.7]
	Sensitivity	$0 < \epsilon < 1$	88.3 ± 1.2 [85.9, 90.4]	68.6 ± 2.2 [63.4, 72.2]	80.0 ± 1.1 [77.7, 82.0]	71.3 ± 1.9 [67.9, 75.4]	80.2 ± 0.5 [79.0, 81.2]
		$1 < \epsilon < 3$	87.3 ± 1.3 [84.5, 89.8]	67.5 ± 2.1 [63.7, 71.5]	80.1 ± 1.0 [78.3, 82.0]	73.8 ± 1.5 [70.8, 76.5]	78.7 ± 0.8 [77.2, 80.4]
		$3 < \epsilon < 10$	88.6 ± 1.4 [85.9, 91.1]	69.4 ± 1.5 [66.6, 72.4]	79.5 ± 0.9 [77.8, 81.3]	73.5 ± 2.5 [67.7, 76.8]	78.1 ± 0.6 [76.8, 79.2]
Non-DP							
Non-DP	AUROC	$\epsilon = \infty$	92.3 ± 0.7 [90.9, 93.5]	77.2 ± 0.3 [76.6, 77.8]	89.3 ± 0.2 [88.9, 89.7]	82.1 ± 0.2 [81.7, 82.5]	88.7 ± 0.1 [88.5, 88.9]
	Accuracy	$\epsilon = \infty$	88.2 ± 1.5 [85.0, 90.7]	71.1 ± 1.5 [67.9, 73.5]	80.7 ± 0.5 [79.5, 81.6]	73.7 ± 0.9 [71.9, 75.4]	79.2 ± 0.3 [78.5, 79.8]
	Specificity	$\epsilon = \infty$	88.2 ± 1.7 [84.7, 90.9]	72.5 ± 1.7 [68.6, 75.3]	79.9 ± 0.7 [78.4, 81.1]	72.2 ± 1.1 [69.9, 74.3]	78.7 ± 0.7 [77.2, 80.0]
	Sensitivity	$\epsilon = \infty$	84.3 ± 1.9 [80.7, 87.9]	69.5 ± 1.7 [66.6, 73.3]	85.0 ± 0.7 [83.6, 86.4]	78.3 ± 1.1 [76.2, 80.6]	82.1 ± 0.7 [80.9, 83.7]

Supplementary Table 2: Fairness evaluation of differentially private ConvNeXt-Tiny models across datasets, privacy levels, and initialization strategies. Fairness is assessed separately across sex and age subgroups using three complementary metrics: AUROC disparity, equal opportunity difference (EOD), and overdiagnosis disparity (OD). AUROC disparity is defined as the absolute difference in subgroup AUROC values. EOD measures the absolute difference in true positive rates (sensitivity) between subgroups, reflecting disparities in disease detection. OD quantifies the absolute difference in false positive rates between subgroups and is computed from subgroup specificities. Results are reported for three initialization regimes (DINOv3, ImageNet, and domain-specific) and four privacy settings ($\epsilon = \infty$, $0 < \epsilon < 1$, $1 < \epsilon < 3$, and $3 < \epsilon < 10$). Metrics were computed from 1,000 bootstrap resamples and averaged across five labels, including atelectasis, cardiomegaly, pleural effusion, pneumonia, and no finding. Results are shown for five chest radiograph datasets: VinDr-CXR (training n = 15,000; test n = 3,000), ChestX-ray14 (training n = 86,524; test n = 25,596), PadChest (training n = 88,480; test n = 22,045), CheXpert (training n = 128,355; test n = 29,321), and UKA-CXR (training n = 153,537; test n = 39,824). Values are presented in percent.

Initialization	Metric [%]	Epsilon	VinDr-CXR		ChestX-ray14		PadChest		CheXpert		UKA-CXR	
			Sex	Age	Sex	Age	Sex	Age	Sex	Age	Sex	Age
DinoV3	AUROC disparity	$0 < \epsilon < 1$	3.3	8.1	0.8	6.3	1.3	8.5	0.2	5.6	0.1	3.4
		$1 < \epsilon < 3$	1.9	9.8	1.1	6.0	1.0	9.1	0.4	4.2	0.5	2.9
		$3 < \epsilon < 10$	2.9	8.1	0.6	7.4	1.9	9.7	0.4	5.7	0.8	3.6
	EOD	$0 < \epsilon < 1$	2.3	29.7	0.5	15.0	2.0	10.8	3.3	6.9	1.1	3.1
		$1 < \epsilon < 3$	6.9	38.2	1.0	4.9	0.1	15.0	8.0	11.3	6.6	1.6
		$3 < \epsilon < 10$	4.4	36.2	1.9	2.2	0.2	11.8	5.4	8.6	0.9	4.5
	OD	$0 < \epsilon < 1$	7.9	10.6	0.1	5.9	1.4	5.7	3.8	2.7	0.4	4.4
		$1 < \epsilon < 3$	4.1	1.2	1.8	1.9	0.7	5.7	7.7	4.5	5.5	5.0
		$3 < \epsilon < 10$	2.0	4.5	0.8	6.3	1.7	3.0	5.3	4.3	2.5	2.9
ImageNet	AUROC disparity	$0 < \epsilon < 1$	1.6	8.7	0.5	5.5	0.7	6.7	1.5	4.1	0.5	2.4
		$1 < \epsilon < 3$	3.3	11.4	0.2	4.3	0.5	6.3	0.6	6.1	0.4	7.6
		$3 < \epsilon < 10$	0.8	9.1	0.2	5.4	0.6	9.8	0.9	7.6	0.4	3.0
	EOD	$0 < \epsilon < 1$	3.1	20.4	0.2	12.6	3.0	2.4	5.7	5.1	0.6	3.3
		$1 < \epsilon < 3$	3.1	33.1	1.0	11.0	3.3	1.8	9.7	20.3	0.2	1.0
		$3 < \epsilon < 10$	5.0	25.6	2.2	18.3	2.5	10.2	1.4	8.1	2.2	2.8
	OD	$0 < \epsilon < 1$	0.2	0.6	0.4	2.9	4.4	12.2	7.2	5.7	0.4	6.3
		$1 < \epsilon < 3$	3.1	3.3	0.3	0.1	2.9	8.8	0.8	2.8	1.1	4.5
		$3 < \epsilon < 10$	4.8	13.7	2.1	1.8	2.5	8.2	2.5	4.9	3.1	3.0
Domain-specific	AUROC disparity	$0 < \epsilon < 1$	1.6	4.5	1.7	5.0	0.1	5.4	0.1	7.8	0.6	3.9
		$1 < \epsilon < 3$	1.2	4.5	1.6	5.5	0.3	5.2	0.7	7.2	0.5	3.2
		$3 < \epsilon < 10$	1.5	4.4	1.5	5.7	0.7	5.3	0.1	7.4	0.5	3.7
	EOD	$0 < \epsilon < 1$	1.2	29.2	0.8	5.9	4.0	5.2	1.7	10.5	1.5	3.2
		$1 < \epsilon < 3$	2.8	29.2	0.3	1.0	2.0	6.5	0.0	11.1	0.2	2.4
		$3 < \epsilon < 10$	1.5	28.5	0.6	2.8	0.8	3.4	4.1	10.2	0.6	4.8
	OD	$0 < \epsilon < 1$	2.9	3.6	2.3	0.2	4.7	6.6	1.4	5.0	2.0	4.0
		$1 < \epsilon < 3$	2.8	6.1	2.8	5.7	3.6	5.0	0.6	1.7	0.4	3.8
		$3 < \epsilon < 10$	2.2	3.8	3.1	3.6	2.1	8.3	4.1	7.4	0.1	2.1
Non-DP												
Non-DP	AUROC disparity	$\epsilon = \infty$	0.9	1.7	5.9	0.8	3.3	0.2	5.4	0.5	4.0	0.9
		$\epsilon = \infty$	27.2	5.9	6.4	0.4	1.8	0.3	3.4	0.4	5.5	27.2
		$\epsilon = \infty$	5.8	3.0	1.1	3.6	6.2	0.4	6.9	0.8	2.8	5.8

Supplementary Table 3: Domain generalization of differentially private ConvNeXt-Tiny models across initialization strategies and privacy levels. ConvNeXt-Tiny models are trained on the combined chest radiograph cohort from five datasets (total training n = 471,896 images) and evaluated on each dataset independently to measure cross domain generalization under differential privacy. The table reports AUROC values (mean \pm standard deviation from 1,000 bootstrap resamples) together with changes relative to the corresponding non private baseline for each initialization strategy (Δ -AUROC). Results are shown for DINOv3, ImageNet, and domain-specific initializations across four privacy settings ($\epsilon = \infty$, $0 < \epsilon < 1$, $1 < \epsilon < 3$, and $3 < \epsilon < 10$). External evaluation datasets include VinDr-CXR (test n = 3,000), ChestX-ray14 (test n = 25,596), PadChest (test n = 22,045), CheXpert (test n = 29,321), and UKA-CXR (test n = 39,824). Values are presented in percent.

Initialization	Epsilon	Metric [%]	VinDr-CXR	ChestX-ray14	PadChest	CheXpert	UKA-CXR
DINOv3	0 < $\epsilon < 1$	AUROC	78.1 \pm 1.1	64.0 \pm 0.3	75.2 \pm 0.3	69.8 \pm 0.2	78.8 \pm 0.2
		Δ from non-DP	-14.2	-13.2	-14.1	-12.3	-9.9
	1 < $\epsilon < 3$	AUROC	78.3 \pm 1.1	64.3 \pm 0.3	75.6 \pm 0.3	69.7 \pm 0.2	79.5 \pm 0.2
		Δ from non-DP	-14.0	-12.8	-13.7	-12.4	-9.2
	3 < $\epsilon < 10$	AUROC	80.2 \pm 1.0	65.6 \pm 0.3	77.0 \pm 0.3	71.3 \pm 0.3	81.8 \pm 0.1
		Δ from non-DP	-12.0	-11.6	-12.3	-10.8	-6.8
ImageNet	0 < $\epsilon < 1$	AUROC	69.3 \pm 1.2	60.4 \pm 0.3	75.3 \pm 0.3	67.9 \pm 0.3	73.2 \pm 0.2
		Δ from non-DP	-23.0	-16.7	-14.0	-14.2	-15.4
	1 < $\epsilon < 3$	AUROC	72.0 \pm 1.1	60.3 \pm 0.3	76.4 \pm 0.3	67.8 \pm 0.3	76.6 \pm 0.2
		Δ from non-DP	-20.3	-16.9	-12.9	-14.2	-12.0
	3 < $\epsilon < 10$	AUROC	79.6 \pm 1.0	63.0 \pm 0.3	76.6 \pm 0.3	69.8 \pm 0.2	81.7 \pm 0.1
		Δ from non-DP	-12.7	-14.2	-12.7	-12.2	-7.0
Domain-specific	0 < $\epsilon < 1$	AUROC	92.5 \pm 0.6	74.9 \pm 0.3	84.6 \pm 0.2	76.0 \pm 0.2	84.9 \pm 0.1
		Δ from non-DP	+0.2	-2.3	-4.7	-6.1	-3.7
	1 < $\epsilon < 3$	AUROC	92.3 \pm 0.5	75.1 \pm 0.3	85.3 \pm 0.2	75.6 \pm 0.2	85.4 \pm 0.1
		Δ from non-DP	+0.0	-2.1	-3.9	-6.5	-3.3
	3 < $\epsilon < 10$	AUROC	92.5 \pm 0.6	75.4 \pm 0.3	85.8 \pm 0.2	76.4 \pm 0.2	85.5 \pm 0.1
		Δ from non-DP	+0.2	-1.8	-3.5	-5.7	-3.2
Non-DP	$\epsilon = \infty$	AUROC	92.3 \pm 0.7	77.2 \pm 0.3	89.3 \pm 0.2	82.1 \pm 0.2	88.7 \pm 0.1

Supplementary Table 4: Demographic fairness under differential privacy across training set sizes on PadChest. The table reports performance through statistical parity difference (PtD) values for ConvNeXt-Small models trained on progressively larger fractions of the PadChest training set and evaluated on a fixed held-out test set ($n = 22,045$). Training set sizes correspond to 10% ($n = 8,821$), 25% ($n = 22,160$), 50% ($n = 44,072$), and 100% ($n = 88,480$) of the available PadChest training images. Results are shown for two initialization strategies (self-supervised DINOv3 and supervised ImageNet pretraining) across three differential privacy regimes ($0 < \epsilon < 1$, $1 < \epsilon < 3$, and $3 < \epsilon < 10$), as well as a non-private baseline ($\epsilon = \infty$). PtD is reported separately for demographic subgroups defined by age groups (<40 years, 40–70 years, >70 years) and sex groups (female, male), and is averaged across five diagnostic labels (atelectasis, cardiomegaly, pleural effusion, pneumonia, and no finding). Values are presented in percent, as mean \pm standard deviation, computed from 1,000 bootstrap resamples.

Initialization	Epsilon	Demographic group	10%	25%	50%	100%
DINOv3	$0 < \epsilon < 1$	Male	2.1	-1.5	-1.4	-1.1
		Female	-2.1	1.5	1.4	1.1
		Below 40	1.9	4.7	4.3	2.6
		40-70	-4.4	5.5	-0.0	1.7
		Over 70	3.7	-9.0	-2.7	-3.6
	$1 < \epsilon < 3$	Male	-2.7	-0.2	-4.5	-2.5
		Female	2.7	0.2	4.5	2.5
		Below 40	4.5	4.1	2.8	4.2
		40-70	6.5	-0.1	-2.1	-1.6
		Over 70	-10.1	-2.4	0.58	-0.9
	$3 < \epsilon < 10$	Male	-0.3	-3.0	0.2	-2.8
		Female	0.3	3.0	-0.2	2.8
		Below 40	3.1	3.6	-2.9	-0.2
		40-70	2.9	1.2	-0.3	-1.0
		Over 70	-5.2	-3.7	2.2	1.3
ImageNet	$0 < \epsilon < 1$	Male	-3.7	-5.2	-1.8	-3.8
		Female	3.7	5.2	1.8	3.8
		Below 40	12.5	5.6	3.6	9.0
		40-70	1.7	3.5	6.9	4.8
		Over 70	-9.7	-7.4	-10.0	-11.0
	$1 < \epsilon < 3$	Male	-5.4	-2.5	-1.4	-3.3
		Female	5.4	2.5	1.4	3.3
		Below 40	11.0	-0.2	10.9	7.5
		40-70	0.1	11.7	0.5	7.1
		Over 70	-7.0	-12.9	-7.4	-12.6
	$3 < \epsilon < 10$	Male	-8.1	-1.8	-3.2	-3.0
		Female	8.1	1.8	3.2	3.0
		Below 40	6.9	8.9	7.4	5.8
		40-70	5.5	1.3	6.3	3.0
		Over 70	-10.5	-7.1	-11.7	-7.0
Non-DP	$\epsilon = \infty$	Male	-1.9	-2.6	-0.8	-0.4
		Female	1.9	2.6	0.8	0.4
		Below 40	1.3	1.5	2.3	3.3
		40-70	3.2	4.2	4.5	4.1
		Over 70	-4.5	-5.6	-6.5	-6.6